White Etching Cracks in wind turbine bearings

Department of Wind Energy Master Report

Antonio Juarez Carrasco

DTU Wind Energy-M-0131

August 2017

DTU Wind Energy
Department of Wind Energy

Authors: Antonio Juarez Carrasco

Title: White Etching Cracks in wind turbine bearings

DTU Wind Energy-M-0131
August 2017

Project Period:
November 2016 – August 2017

ECTS: 45

Education: Master of Science

Supervisors:

Hilmar Kjartansson Danielsen
DTU Wind Energy

Kristian Vinter Dahl
DTU Mechanical Engineering

Remarks:
This report is submitted as partial fulfillment of the requirements for graduation in the above education at the Technical University of Denmark.

DTU Wind Energy is a department of the Technical University of Denmark with a unique integration of research, education, innovation and public/private sector consulting in the field of wind energy. Our activities develop new opportunities and technology for the global and Danish exploitation of wind energy. Research focuses on key technical-scientific fields, which are central for the development, innovation and use of wind energy and provides the basis for advanced education at the education.

We have more than 240 staff members of which approximately 60 are PhD students. Research is conducted within nine research programmes organized into three main topics: Wind energy systems, Wind turbine technology and Basics for wind energy.

Technical University of Denmark
Department of Wind Energy
Frederiksborgvej 399
4000 Roskilde
Denmark

www.vindenergi.dtu.dk

White etch cracks in wind turbine bearings

Master of Science Thesis

For obtaining the degree of Master of Science in Engineering
Wind Energy at Technical University of Denmark
Aerospace Engineering at Delft University of Technology

Antonio Juárez Carrasco

European Wind Energy Master - EWEM
Wind Energy Department, Technical University of Denmark
Faculty of Aerospace Engineering, Delft University of Technology

European Wind Energy Master - EWEM

Of

Rotor Design Track

The undersigned hereby certify that they have read and recommend to the European Wind Energy Master - EWEM for acceptance a thesis entitled “White etch cracks in wind turbine bearings” by Antonio Juarez Carrasco in partial fulfillment of the requirements for the degree of Master of Science.

Dated: 29 May 2018

Supervisor: _____

Dr. Ir. Hilmar K. Danielsen of Technical University of Denmark

Supervisor: _____

Prof. Dr. Ir. Roumen H. Petrov of Delft University of Technology

Abstract

Wind turbine (WT) gear boxes are prone to failure well below the expected 20 years' lifetime of a WT. It has been identified that most of the failures observed are due to white etch crack flaking. Although this type of failure has been intensely studied, the underlying mechanisms have not been identified; however, recent advances have shown that non-metallic inclusions might act as crack initiators. In this work, different bearings presenting this type of damage will be examined via microtomography scans and high precision serial sectioning to reveal surfaces displaying crack-inclusion interactions. Furthermore, by means of energy dispersive X-ray spectrometry it will be possible to investigate the chemical composition of the non-metallic inclusions. The findings will be compared to current initiation and propagation theories proposed in literature; Thus, this study will add experimental observations to current investigations using a novel technique.

Contents

List of figures

List of tables

Acronyms

AISI	American iron and steel institute
BCC	Body-centered cubic
DER	Dark etch regions
EBSD	Electron backscatter diffraction
EBSP	Electron backscatter pattern
EDS	Energy dispersive X-ray spectrometry
OM	Optical microscope
OPS	Oxide polishing suspension
PAGB	Prior austenite grain boundary
RPM	Revolutions per minute
SEM	Scanning electron microscope
WEA	White etch area
WEC	White etch crack
WSF	White structure flaking
WT	Wind turbine

1. Introduction

1.1. Motivation

A worldwide increase of energy demand, global uncertainty in fossil fuel supply and concerns for the environment has resulted in the growth of renewable energy technologies. The wind energy sector has experienced a rapid increase in the installation of wind turbines, either due to government funding or growth in the private sector, owing to the necessity of finding another source of large scale energy production. The U.S. government alone committed that by 2030 at least 20% of their energy production will be from renewable sources [1]. In this rapid growth of demand manufacturers had to find commercially available components without being thoroughly tested. Thus, the reliability of wind turbines falls short from the 20-year operational lifetime goal. An example of such vulnerable components is regularly seen in the gearbox, which in some cases need to be replaced after only 3-5 years of operation, the downtime and cost of parts can well up add up to 10% of the total original construction cost [2]. The expected operational life of a gearbox is well above 20 years, these usually are a derivative of maritime technology, however they do not encounter the operational conditions of wind turbines. Additionally, recent statistics from the US Department of Energy and National Renewable Energy Laboratory showed that approximately 76% of gearbox failures were caused by bearings [2], mostly in the intermediate and high speed stages. Over the last 20 years horizontal axis wind turbines power output has increased from 50 KW, in the early stages, to 8 MW; this has been largely due to the increase of the rotor diameter from 15m to 164m. During this period, various manufacturers have decided to incorporate the gearbox into their design. This element is needed because the tip velocity of the blade is designed to ensure it will not exceed the speed of sound, resulting in an overall slower rotational speed. The blades are connected to the lower speed shaft, which is coupled to the gearbox which increases the rotational speed of a secondary shaft (high speed shaft) that is subsequently connected to the electric generator to comply with grid requirements as shown in Figure 1.

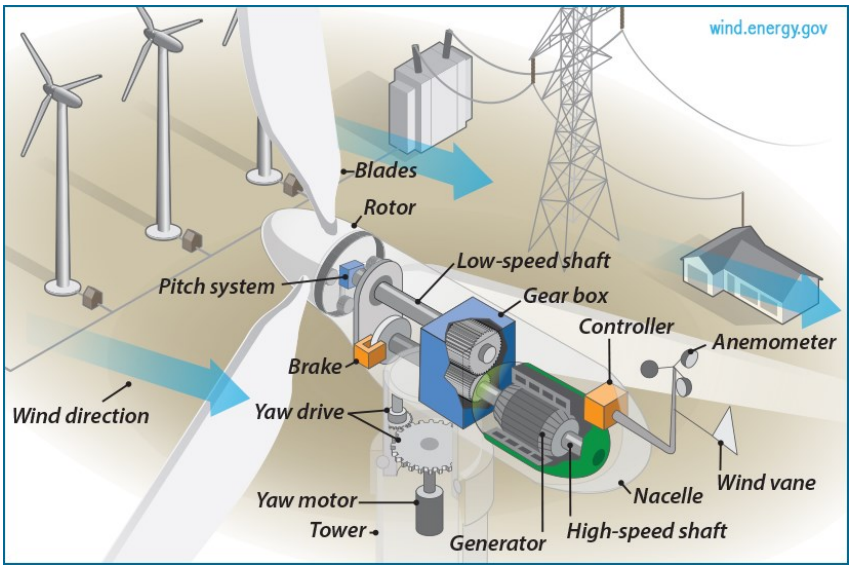

Figure 1 Wind turbine main components

Despite the complexity of adding an extra component and the high percentage of failures, this design has become widely used in the industry [3]. As previously discussed most of the gearbox failures are attributed to bearings, although failure in electrical components are much frequent the former has a higher repair cost [4]. One of the failure mode that has been observed in bearings is white structure flaking (WSF) and it has been reported to appear within 6-24 months [2] [5], its main mechanisms are driven by micro-structural changes and the formation of cracks that when etched under nital (2% nitric acid in ethanol) and viewed under a bright field appears to have a lighter color than its surroundings [6]. Steels for this application usually consists of AISI 52100 100Cr6 which have carbon concentrations within 0.98-1.10 wt.% (percentage in weight) and substitutional solute content less than 3 wt.%. as defined in Table 1.

Element (wt%)

C	Mn	P	S	Si	Cr
0.98-1.10	0.25-0.45	0.025	0.025	0.15-.0.35	1.30-1.60

Table 1 AISI 52100 100Cr6 chemical composition [7]

WSF is observed on steels that are through hardened from austenite, either by martensitic or bainitic, and case hardened steels [8]. For the case of larger bearings other methods are used such as carburization or increased concentrations of alloying elements. As a result, these materials have a high endurance to wear and fatigue. Rolling contact fatigue is defined as material removal driven by crack propagation caused by the near-surface alternating stress field; it is known that in a properly lubricated bearing and under normal operational conditions (no overloading, no chemical influences or electric currents) this failure is not present [5]. Nevertheless, rough surfaces increase the complexity and interaction of the stress fields, so it comes as no surprise that the root cause of this failure mode is still being investigated and proposed theories are still highly contested.

The operational pressure on the high-speed shaft cylindrical roller bearing is within a range of 1,200-1,500 MPa, relatively low compared to its fatigue limit. Since the bearings are not being exposed to overloading they should not present white etching cracks, therefore some authors have proposed the following theories: hydrogen diffusion, hammering-like impact creating plastic deformations near inclusions, electromagnetic/thermal induction [9] and shear stress induced fatigue [10]–[13]. Some sources of hydrogen intake can be water, corrosive impact, lubricants, and additives. In addition, atypical operational conditions of wind turbines, such as wind gusts, turbulence, and other meteorological phenomena, contributes to the misalignment of the drive train and subsequent stick-slip mode damages resulting in microcracks and unusual shear stress concentrations [14]. Recent investigations argue that non-metallic inclusions do not play a role as initiators and point out that an accumulation of plastic deformation in the microstructure as the main reason [10]. While others argue that non-metallic inclusions are the main source of crack initiation, as it has been observed for the case of “butterfly” cracks. Nevertheless, white etch cracks (WEC) are not restrained only to butterfly cracks but also complex crack networks [15] [16]. Overall, no support or agreement has been made regarding if white etch areas (WEA) appear after or before the crack.

1.2. Problem statement

The objective of the present work is to investigate five bearing samples by 3D X-ray microscopy, a non-destructive method able to map cracks and inclusions. Afterwards, serial cross sectioning will be performed to reveal on the surface a specific inclusion-crack interaction and by means of energy-dispersive X-ray spectroscopy (EDS), investigate the chemical composition of the inclusions. For some samples, further investigation via electron backscatter diffraction (EBSD) will be performed to further investigate the path of the crack and the microstructure around the white etch area. The results will then be compared to proposed root causes found in literature and Hertzian contact stress theory.

2. Rolling contact fatigue

This chapter aims to illustrate the driving mechanisms of rolling contact fatigue; the main characteristic of this failure mode is that it starts with the formation of white etching cracks (WEC) and although they have been lengthily described in literature, the root causes are still not well established, but they are characteristically different from typical wear. First, three theories describing WECs will be revised, all three theories have been confirmed by different researchers, but no final consensus has been reached. It is expected to observe some features supporting one of them during experimentation. Furthermore, a mathematical model will be introduced as to explain where the maximum stress concentration is located and the theory behind sub-surface crack initiation. The chapter will continue explaining cyclic stress concentrations which will result in dark etching regions (DER). Finalizing with an overview of macro pitting, which results in the fatal failure of the bearing.

2.1. White etching cracks

The phenomenon of steels etching differently after cyclic loading was observed as early as 1945 [17], where the author reported the existence of some "grey lines". However it was in the 1960's that a group of researches coined the term "white etch area" (WEA) [18]. The observed WEAs are either at the crack tip or next to them and will cause some of its material to spall in the form of flakes introducing foreign particles into the lubricant and causing further damage. The spalling of flakes due to WECs failure mode are usually observed within 1%-10% L_{10} life of the bearing, dramatically cutting down their lifespan [15]. White etch cracks usually range from 0.1-1 μm in width and appear in the subsurface of the rolling surface within a depth of 0.2-1.0 mm [15]. WECs are defined as cracks in the material that when etched by nital and observed under a bright field some of the adjacent area appears brighter. These areas remain unaffected by the etching process and start as micro cracks in the subsurface, located on areas with the highest concentration of shear stress. As mentioned earlier the white etched areas have no microstructure and it is mostly compromised of nano-grains; it is also reported to be supersaturated with dissolved carbon making it more brittle and harder than the surrounding steel matrix [19]. It was suggested that WEAs are formed only at "butterfly cracks", but new evidence has suggested that accumulated dislocations, due to shear stress, forms these areas to release some of the strain energy; explaining why inclusions, voids and large carbides are recurrently found adjacent to WEAs [20]. Overall it has been observed that WECs initiate and propagate with a directionality of 30º-50º and 130º-150º from the over-rolling direction [21]. The propagation seems to initiate from inclusions, given the impression of butterfly wings viewed from a 2-D plane. Butterfly-shaped cracks are frequently reported to start on sulfite inclusions, nevertheless, voids and carbides are also able to propagate butterfly-like cracks and aid in the development of complex crack networks.

It is important to note that the driving mechanisms are different and depend on the type of steel, bearing, application, lubricant, etc. Hence, a general root theory for WECs has not yet been

postulated, instead three theories will be described. The first one argues that WECs are caused by hydrogen uptake. It has been observed that hydrogen adheres on to the microstructure of the steel, such as grain boundaries, voids or dislocations [10]. This in consequence degrades the strength of the material and increases the chance of plastic deformation at operational stresses. There has been extensive research demonstrating that by artificially loading a steel specimen with hydrogen, it will show an increase of WECs compared to non-charged specimens. A second theory argues that stresses from stick-slip mode produce micro cracks on the surface, which will be subsequently filled up by the lubricant. It has been reported that at the tip of these microcracks the lubricant degrades into hydrogen and by means of vibration the hydrogen penetrates the subsurface and is pinned as previously described. The main difference from the first and second theory is that the main drivers for the latter are vibrations and micro damage on the surface while in the former, the main driver is hydrogen diffusion. A third theory argues that the large plastic deformation, characteristic of WECs, are due to pulses in the raceway, creating adiabatic shear bands. These pulses are common in ballistic impact caused by cavitation and can lead to crack growth within the material [16].

2.2. Stresses from rolling contact

The loads that rolling elements and raceways undergo during operation tend to be high due to small contact areas between bodies. It is common for a bearing to experience stresses exceeding 1,380 MPa during operation, furthermore, some specialized bearings are tested under loads that exceed 3,450 MPa [22]. The stress fields that are observed in the components of the bearings tend to dissipate rapidly, mostly affecting regions near the surface. Hence, special attention has been placed on the surface or subsurface of the components as to prevent damage. The following analysis will not be extensive, but the results will give a representation of the damage observed during the experiments. As an initial step and ease of solution it is assumed that the bodies in contact are only subjected to elastic deformation, the material is frictionless, and the raceway is smooth. For two bodies being pressed together and by letting R_1 and R_2 be the radii of the surface curvature as shown in Figure 2 b), the relative curvature can be obtained by $(R_1^{-1} + R_2^{-1})^{-1}$.

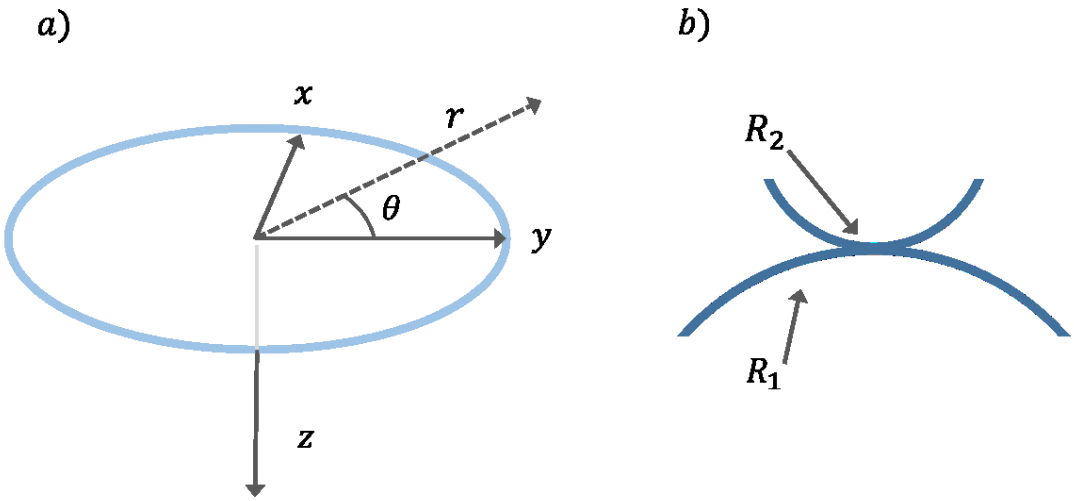

Figure 2 a) Definition of coordinates b) Radii of surface curvature

It will also be assumed that the contact area between the bodies will have a circular shape with radius, r_0, and the pressure exerted on the bodies will be then given by p, in terms of distance r then the following equation can be obtained;

$$p = -\sigma_z\{z=0\} = p_0\sqrt{1-\frac{r^2}{r_0^2}} \quad where \;\; r_0 = \left(\frac{3wR}{4E^*}\right)^{\frac{1}{3}}$$
$$and \;\; \frac{1}{E^*} = \frac{1-\nu_1^2}{E_1} + \frac{1-\nu_2^2}{E_2} \qquad \textbf{Eq. 1}$$

Where, E_n and ν_n are the Young's modulus and Poisson's ratio respectively and the subscripts indicate the difference of material properties and w is the applied load. The following relations correspond to the radial and tangential stresses within the contact circle and are given by [4];

$$\frac{\sigma_r}{p_0} = \frac{1-2\nu}{3}\frac{r_0^2}{r^2}\left(1-\left[1-\frac{r^2}{r_0^2}\right]^{\frac{3}{2}}\right) - \sqrt{1-\frac{r^2}{r_0^2}}$$
$$\frac{\sigma_\theta}{p_0} = \frac{1-2\nu}{3}\frac{r_0^2}{r^2}\left(1-\left[1-\frac{r^2}{r_0^2}\right]^{\frac{3}{2}}\right) - 2\nu\sqrt{1-\frac{r^2}{r_0^2}} \qquad \textbf{Eq. 2}$$

The stresses outside the contact circle can be obtained by;

$$\frac{\sigma_r}{p_0} = -\frac{\sigma_\theta}{p_0} = \frac{1-2\nu}{3}\frac{r_0^2}{r^2} \qquad \textbf{Eq. 3}$$

The stresses along the z-axis, defined as defined in Figure 2 a), at $r = 0$ are given by [23],

$$\frac{\sigma_r}{p_0} = \frac{\sigma_\theta}{p_0} = -(1-\nu)\left(1-\frac{z}{r_0}\tan^{-1}\left\{\frac{r_0}{z}\right\}\right) + \frac{1}{2}\left(1+\frac{z^2}{z_0^2}\right)^{-1}$$
$$\frac{\sigma_z}{p_0} = -\left(1+\frac{z^2}{z_0^2}\right)^{-1} \qquad \textbf{Eq. 4}$$
$$\tau = \frac{1}{2}|\sigma_z - \sigma_r| \;\; where \;\; \tau_{max} = 0.31\,p_0 \;\; @\; z = 0.48\,r_0 \;\; and \; \nu = 0.33$$

The solutions of the previous equations can be seen in Figure 3.

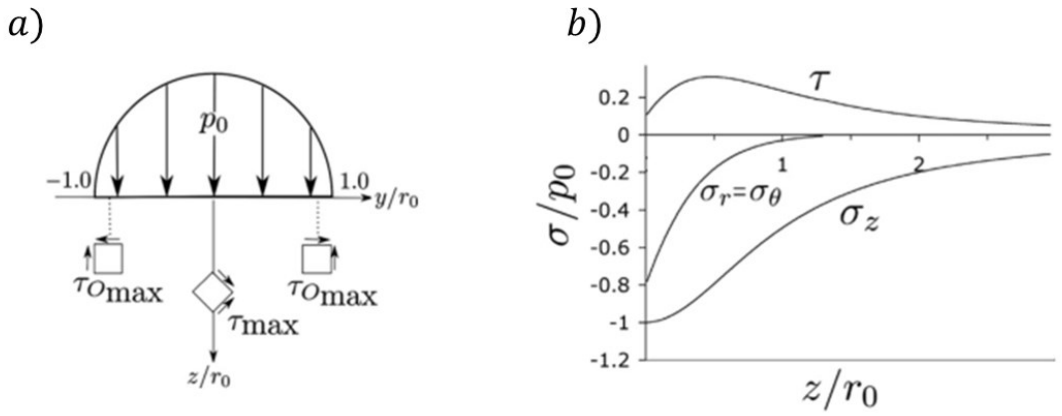

Figure 3 a) Maximum shear stress and orthogonal shear stress over an area of radius r_0 b) Normalized stress as function of z/r_0 along z-axis ($r = 0$) [4]

Furthermore, once the orthogonal stresses are retrieved a failure criterion can be applied, von Mises stress criterion can be obtained as;

$$\sigma_v = \frac{1}{\sqrt{2}}\left[(\sigma_{\theta\theta} - \sigma_{rr})^2 + (\sigma_{rr} - \sigma_{zz})^2 + (\sigma_{\theta\theta} - \sigma_{zz})^2 + 6\left(\tau_{\theta r}^2 + \tau_{rz}^2 + \tau_{\theta z}^2\right)\right]^{\frac{1}{2}} \quad \textbf{Eq. 5}$$

The solution of the previous equation is given in Figure 4.

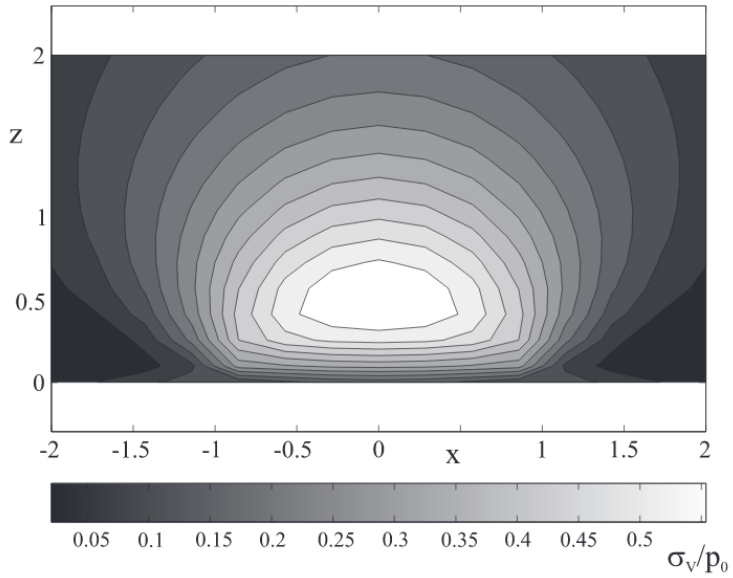

Figure 4 Von Mises stresses (x-z plane) [24]

It can be observed that under this criterion the maximum stress concentration is located internally of the elastic medium and it is diminished throughout the rest of the body. Although only a circular contact geometry was discussed, additional contact geometries can be found in [23].

2.3. Dark etching regions

Under ideal operational conditions bearings should not experience residual stresses nor damage, this is achieved if the strains during cyclic loading are below the plastic yield of the material. However, it has been observed that WECs show large plastic deformations along with a dark etching region. There have been numerous reports studying the microstructural changes during rolling contact fatigue, consistently reporting a martensite decay, referred as "dark etching region" (DER) due to the aggressive attack of nital when etched. Of interest is the study of Swahn [6] where he listed a terminology for the various stages observed during his experiments. He reports that DER first appears between 10^7 and 10^8 cycles but depends on loading of the bearing. After 10^8 he reports the appearance of 30° bands tangentially located with respect the raceway. The driver for the directionality of these bands is clearly dependent on the rolling direction and can only be assumed that is independent of the crystallographic orientation of the matrix. After 5×10^8 cycles he reported the presence of a second band, this time with a tangential angle with respect the raceway of 80°, these bands intersected the previous 30° bands and once more were dependent on the rolling direction. As these secondary bands developed he consistently reported a decay of the martensite leading to ferritic regions mixed with carbide-like regions and residual martensite. Even though no mention of grain size is referred in this study, modern crystallographic techniques report nano-size grain structures in regions that undergo large plastic deformations. Although there is some stress relief on the raceway after initial plastic strain as well as work hardening on the surface, the overall subsurface shows a sharp softening, measured by a Vickers hardness test and shown in Figure 5.

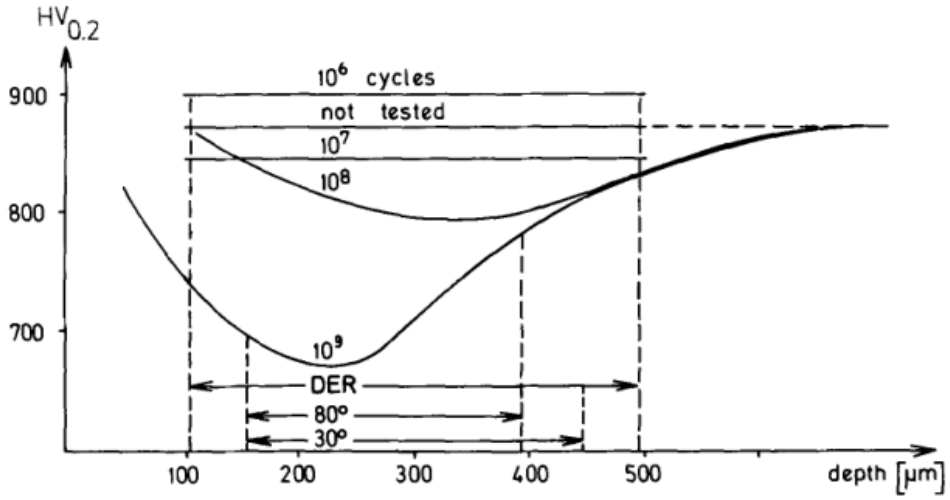

Figure 5 Vickers hardness vs depth after incremental cyclic loading [6]

2.4. Macro pitting

Despite extensive research on the field, there is no current model able to predict crack initiation, but some attempts to describe butterfly cracks has been done [25]. The complex interaction of various factors makes prediction of cracks a complex task, but it has been observed that shape, size, adhesion between inclusions and the matrix, difference in Young's modulus and thermal expansion coefficients are regarded as the main parameters for crack initiation [8]. These cracks can propagate along grain boundaries of the matrix or inside inclusions, but it has also been observed that cracks propagate along the inclusion-matrix interface. This behavior has been extensively described in the literature and different theories and predictions have been made. Regardless of the initiation or growth, when cracks reach the surface some of the material spalls, contaminating the lubricant and subsequent pits are formed on the raceway. At this stage, the bearing is considered as failed; although the life of the bearing can be described in terms of cycles before the spalling process, this type of damage is not noticeable until the sub-surface cracks reaches the surface and so the crack propagation which started as individual micro-cracks might well have developed into a complex crack network. Furthermore, the pits will be cyclically loaded by the rollers during operation, creating stresses in the order of 2 GPa [26], and further increasing the damage on the surface. It has been observed that the leading edge of the initial pit will remain unaffected, while wear damage will propagate along the rolling direction as shown in Figure 6.

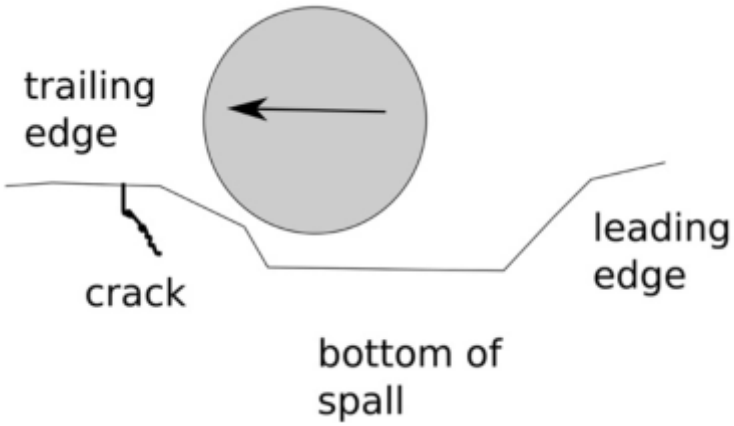

Figure 6 Schematic illustration of damage propagation [27]

It is the aim of this research to observe and report the crack propagation and the interaction between non-metallic inclusions and voids. Evans has reported that such undertaking has relied on guessing the location of damaged areas. Even if guessed correctly, only a 2-D plane of the crack can be observed, though it may be a 3D network [8]. The presented methods for 3D mapping of crack networks have been either by means of focused ion beam (FIB) or serial sectioning, both methods repeatedly micro machine a thin slice of the sample and capture an image of the revealed surface. Only after a considerable set of images is obtained, it can then be reconstructed into a 3D model with the appropriate software, these methods are time consuming and destructive [15]. Instead, a micro-tomography scan would be used on different samples to investigate crack-inclusion interactions and propagation path. The results will then be validated by means of serial sectioning, allowing the study of the chemical composition of the inclusions by an energy-dispersive X-ray spectroscopy.

3. Experimental set-up

The main technique used for 3D reconstruction of cracks are based on images obtained by serial sectioning, where a thin slice of the sample is removed, then an image of the revealed surface is recorded, and finally reconstructed in a 3D model by a suitable software [15] [28]. Serial sectioning limits the possibility of sample investigation after the 3-D model has been created due to its destructive nature. In contrast, the proposed technique in this investigation, X-ray micro-tomography, offers the possibility of inspecting the sample after the 3D model has been constructed. Although referred as a nondestructive technique, x ray micro-tomography does require samples to be machined from the bearing in a needle-like shape. For better imaging resolution, samples should be as transparent as possible to the X-rays used, the sample itself is not affected by the x-irradiation hence the term nondestructive. The resolution of the tomography is limited in the size of both the specimen and the crack. Ultrasound is also widely used in the detection of cracks, often validated through serial sectioning, and has become an industry standard for monitoring in field bearings [29]. The experimental research will be conducted in DTU, Wind Energy Department. The experimental setup will consist of the following stages:

3.1. Optical microscopy (OM)

Potential regions of interests were machined and hot mounted in a polymer matrix, this process was done in the Labo Press 3 at a setting of 150°C for 5-7 minutes and a compression force of 15-20 kN in either Polyfast or Condufast matrix, the sample was then cooled for 5-6 minutes before being removed. Grinding was done in the Struers Rotopol-22 from SIC 220 to SIC 4000 in intervals of 3-5 minutes and an applied load of 15-20 N, finally the surface underwent 3 diamond polishing stages (9µm, 3 µm and 1 µm) to obtain a scratch free surface, this was performed in the same Struers machine until a flattened surface was obtained, the same grinding settings were used. During each stage, the sample was thoroughly cleaned to prevent contamination from coarser abrasive grains into the finer grinding or polishing stages. This was done either by automated water rinsing and centrifugally dried or cleaned ultrasonically in an ethanol solution and dried by compressed air, the latter method was preferred in the polishing stages as to prevent oxidization of the sample. The Leica optical microscope is equipped with a MC120 HD camera and was used for initial investigations and imaging. Most of the samples were etched with nital in steps of 5 to 10 seconds; after this stage, the WECs became visible. For cases where the etching was too aggressive the nital solution was further diluted (1% nitric acid in ethanol) and the time steps consisted of 3-5 seconds.

3.2. Serial sectioning

Currently there are two methods available to perform a high precision polishing at DTU; the first one can be done using the Logitech PM5D Precision Polishing and Lapping System. The main advantage of this technique is the control of the material being removed by the user. In general, the lower the RPM of the lapping plate the slower the rate at which the sample material will be removed, but it is dependent on a continuous abrasive feed. Also, it would be ideal to obtain a mirror like finish for view under the optical microscope (OM) during the material removal process and intermediate steps as to know the position of the serial cross sectioning. Unfortunately, it was not possible to obtain this finish with the Logitech PM5D as various issues arose during its operation and some extra accessories were needed for samples with a height larger than 3 cm, also a special base for the sample holder is necessary to measure the force it is exerting on the sample being grinded. Hence, a second method was developed to do the serial sectioning, this consisted of using the current Struers Rotopol-22 and characterize the depth of the material being removed using two grain sizes of diamond polish powder (3µm and 1µm). This was done by first applying a Vickers hardness indent and measuring the diagonal length of the indent mark. After the indent is made two right triangles are formed from the vertex of the indenter with an inclined plane of 22° with respect the horizontal plane as shown in Figure 7.

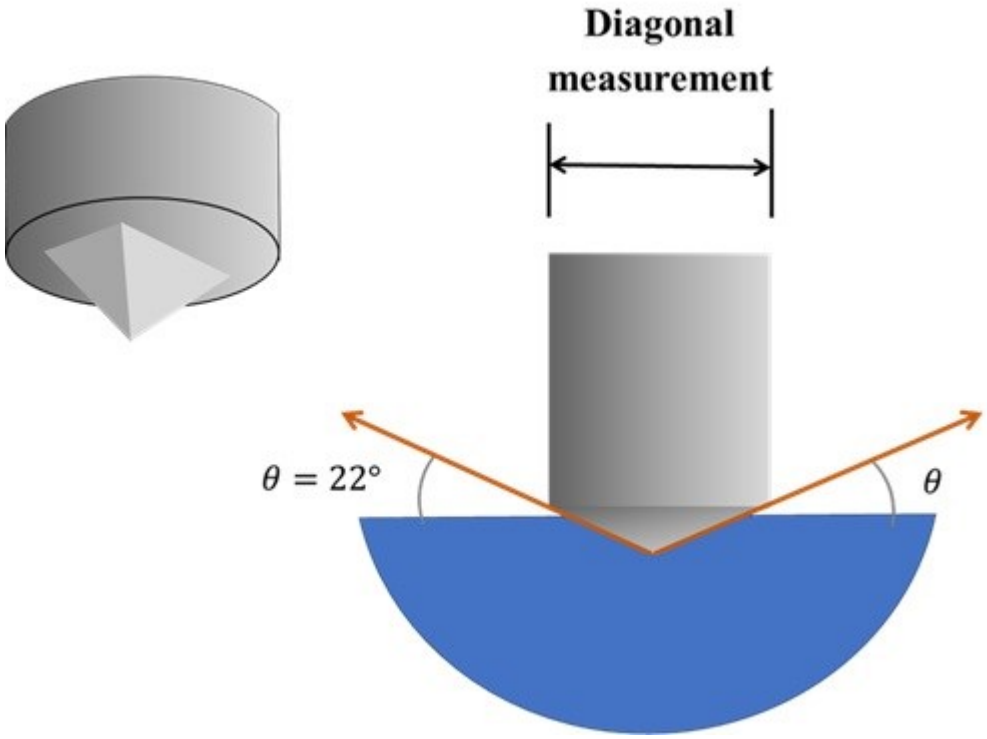

Figure 7 Schematic of Vickers hardness indent

Half of the diagonal measurement (DM) will be adjacent to the known angle θ, thus the depth of the indent can be obtained by $depth = 0.5\ DM \tan\theta$. As the base decreases in size during

the polish, the depth of material being removed can be inferred by re-measuring the diagonal length of the indent. Three measurements are shown in Figure 8 as illustration of this process.

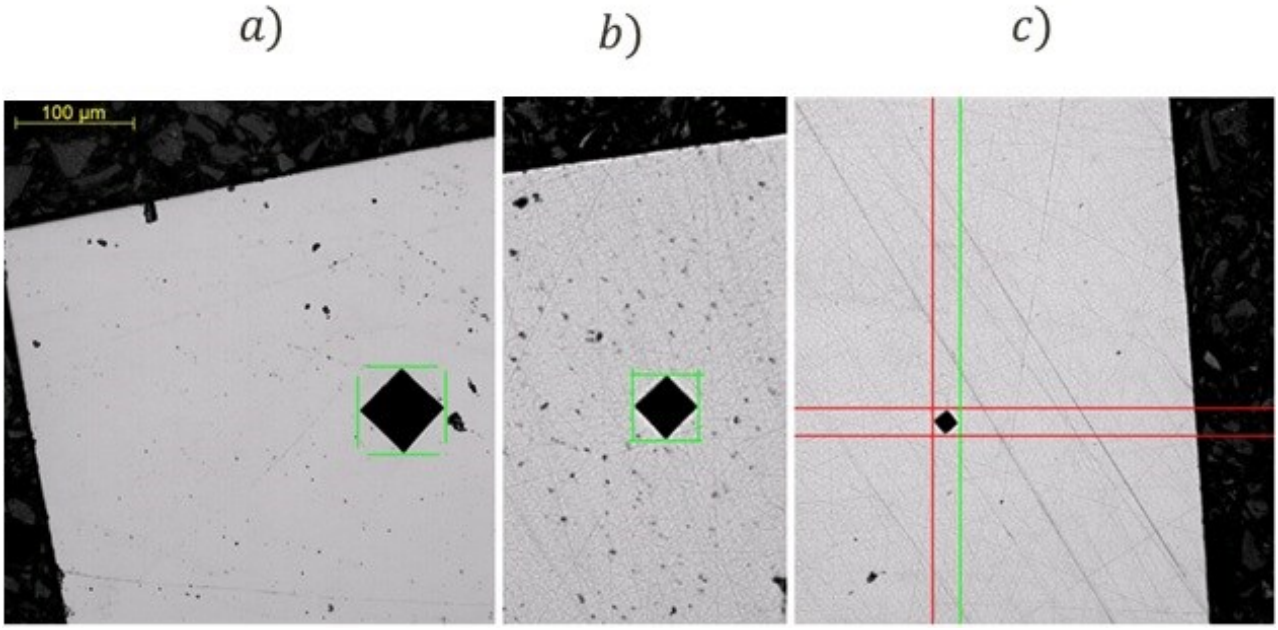

Figure 8 Progression of polishing using Struers Rotopol-22

The original hardness indent had a starting value of 74 µm (a), after polishing with a load of 15 N for 2 minutes the diagonal was reduced to 54 µm (b), the sample was re-polish for 3 minutes with the same settings resulting in a final measure of 23 µm (c). Not shown in Figure 8 but the procedure was repeated for 60 and 30 seconds and same settings. Finally, a grain size of 1 µm was used and the procedure was repeated for two and three minutes; the results are presented in Table 2.

	Depth (µm)	
Time (s)	Grain size of 3 µm	Grain size of 1 µm
180	7	1
120	4	0.5
60	3	--
30	1	--

Table 2 Depth characterization results

It was observed that this characterization had to be done for each specimen as the steel exposed had a different surface area and the polishing depth was not the same. Also, as residue of previous polishing stages was deposited on the polish cloth the process became less efficient and the cloth needed to be replaced or cleaned to obtain similar results as when the characterization measurements were made. The Struers Rotopol-22 is normally used to polish samples to view under the OM, hence intermediate steps during serial sectioning required at most an extra 1 µm diamond polish. For larger steps of material removal (>50 µm), the samples were grinded using the finer grinding paper available (4000 SiC) under a load of 15-20 N in stages of 2-3 minutes. To achieve the desired depth of the material being removed four points on the sample were measured with a digital micrometer. This process left a rough surface, but

additional steps of polishing were taken and compared to the tomography results to orient and confirm the revealed surface of the sample.

3.3. Scanning electron microscope (SEM)

The HITACHI TM3000 tabletop scanning electron microscope (SEM) was used in this investigation mainly to perform energy dispersive X-ray spectrometry. The basic principle is that an electron gun produces a beam of high energy electrons which will be aimed at a conductive surface and, as the name suggests, scanned across the sample. Unlike the OM it does not produce a real image of the sample but rather is the result of a beam probe illuminating the surface in multiple positions. The resulting signal is generated from the reflection and detection of bouncing electrons and via a scintillator the electron detector can convert the electrons to photons. The signal captured by the electron detector will indicate topographic differences on the surface. A photomultiplier is needed to amplify the signal coming from the scintillator and convert it into an electrical signal to modify the intensity on the screen, obtaining the characteristic large depth of field 3D images [30]. Figure 9 schematically shows the basic layout of the SEM.

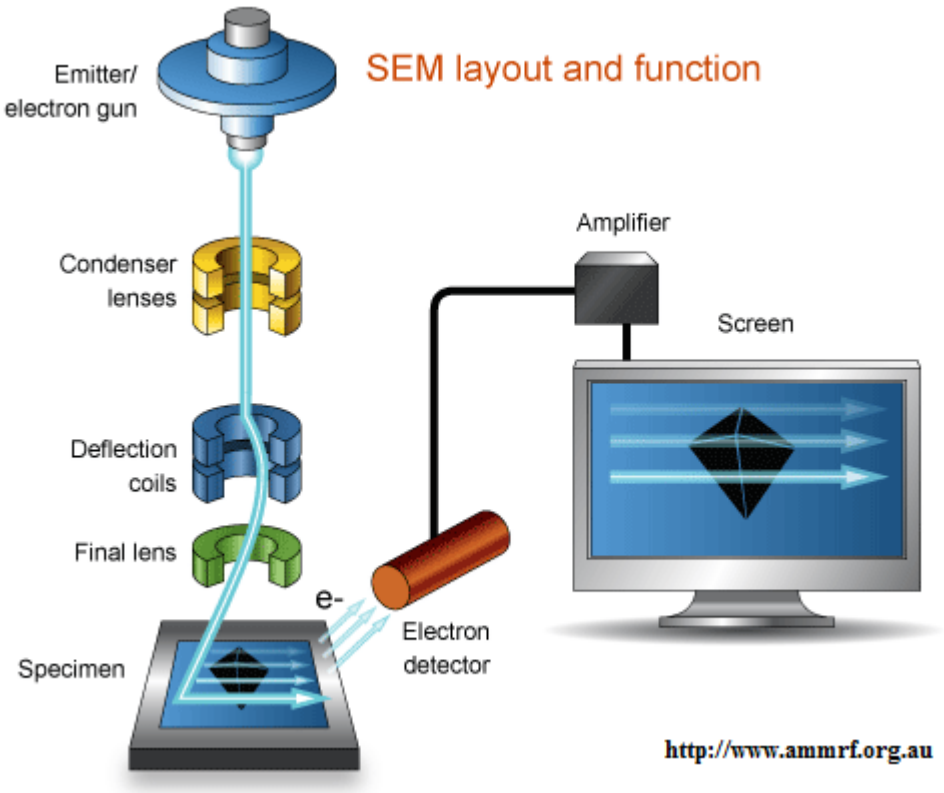

Figure 9 Basic SEM layout

3.4. Energy dispersive X-ray spectrometry (EDS)

Once a surface of interest is revealed by the serial sectioning, guided by the 2D images of the tomography, a chemical analysis will be performed to investigate the composition of the inclusions. Energy dispersive X-ray spectrometry (EDS) bombards a focused beam of electrons in a vacuum sealed chamber to obtain a quantitative chemical composition. The three basic components for this configuration are the X-ray detector, besides detecting incoming reflected X-rays from the sample it also transforms the input into electronic signals; the pulse processor, it analyzes and measures the incoming electromagnetic signals and determines the energy of each X-ray; finally, the multiple channel analyzer, interprets and visually displays the results [31]. It is important to note that although the surface is bombarded some of the X-rays picked by the detector will be from a volume deeper than the surface, coming from secondary and backscatter electrons as shown in Figure 10.

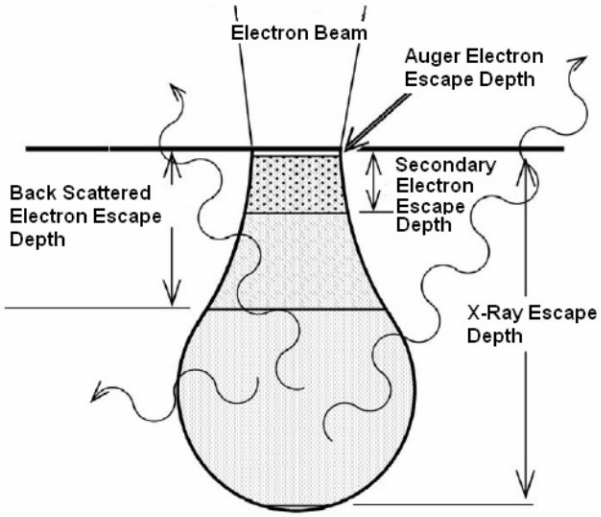

Figure 10 Schematic X-ray escape depth [31]

The HITACHI TM3000 tabletop scanning electron microscope (SEM) equipped with the Bruker Quantax 70 EDS system will be used for this investigation. The scanning beam of the SEM can map a specific area rendering images with element concentrations based on the X-ray spectra obtained by the detector, alternatively only a single line read can be obtained if desired. Although the SEM is designed to produce electron images, it can be used for element mapping, line scanning and point analysis if an X-ray spectrometer is added. Since fine polishing and material removal will be done to reveal a surface of interest no further sample preparation will be required. For this type of analysis, it is desired that the surface roughness of the sample does not affect the results.

3.5. Electron backscatter diffraction (EBSD)

By means of accelerated electrons from the main beam of a scanning electron microscope (SEM), it is possible to obtain information of the lattice in crystalline materials. These electrons are diffracted and can be detected when they collide on a phosphor screen generating visible lines called Kikuchi bands or electron backscatter pattern (EBSP). The patterns are projections of the lattice planes from the crystalline sample that when cross referenced with data, including crystallographic information for the phases of interest, it is possible to identify phases based on the crystal structure. It is of great aid to know the type of crystallographic structure of the sample before the study is made so that the correct data set is chosen. Special sample preparation is required after grinding and polishing since it experiences a large stress relief and so the exposed layer needs to be removed. This was done by polishing the sample during 30 minutes under 1µm OPS colloidal silica under a low applied load, less than 15 N. The sample needs to be immediately washed, then it was cleaned with a soft tissue, flushed with ethanol and dried with pressurized air. The SEM Zeiss SUPRA 35 with an Oxford Instrument EBSD detector was used to make the study. The final sample is placed in the SEM with an inclination of approximately 70° relative to the incidence of the electrons' beam as shown in Figure 11.

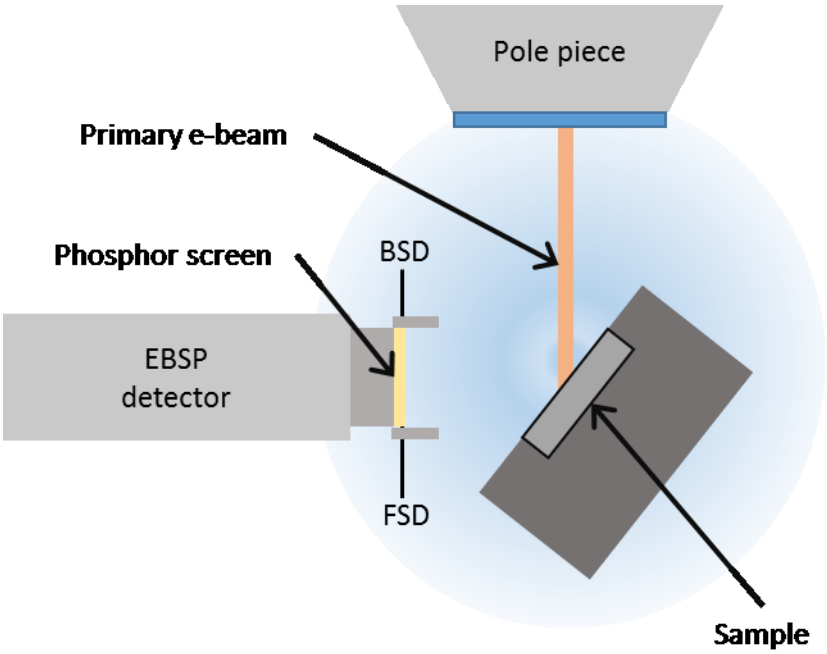

Figure 11 Schematic illustration of sample positioning towards EBSP detector [32]

The EBSP is supported on a horizontal mobile carriage, and for optimal results it should be placed as close to the sample while avoiding a collision between the phosphor screen and the surface of the sample. The pattern lines are electronically digitalized and the raw data is then processed by the following software: Mambo (inverse pole figures), Tango (mapping) and Salsa (orientation distribution functions) [33]. If the size of the grain is outside of the resolution range of the equipment it will not index that area, usually this is visualized by a black region when the results are colorized.

3.6. Tomography scan

X-ray tomography is a 3D imaging technique that allows to visualize the inner components of a body, assuming it is composed of a non-homogenous material and they have an X-ray absorption coefficient different from that of the surrounding matrix. The difference in absorption is proportional to the difference in mass density. The aim of this experiment is to observe crack-inclusion interactions with the highest spatial resolution. Hence the size of the samples was limited, this is due mainly to two factors, the first one being that the size of the sample affects the choice of the energy of the photons, as a rule a minimum of 30% of the intensity of the incident beam should remain re-transmitted throughout the specimen to obtain an optimal set of images. This can be achieved by further increasing the energy of the photons, but lower energy levels are required to keep a good contrast of absorption between the voids or inclusions and the surrounding matrix, lower levels of energy also increase the efficiency of the X-ray detector. These conflicting requirements were fulfilled individually for different samples. The second limiting factor is that the sample must remain within the field of charge (X-ray beam), this depends on the size of the specimen, the optical magnification, and the desired voxel size in the reconstructed 3D model. The schematic of the experimental set up is shown in Figure 12.

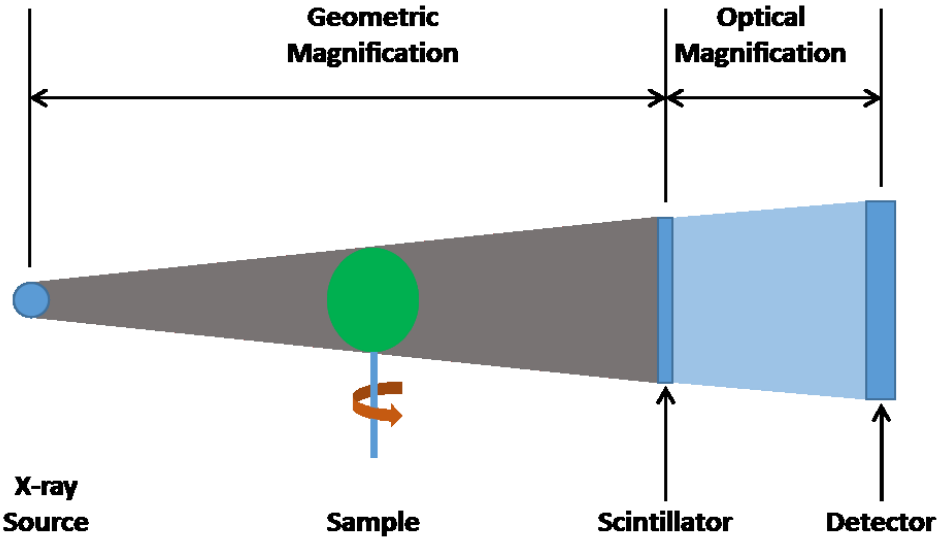

Figure 12 Schematic illustration of micro-tomography experiments [34]

Throughout the experiments the effective voxel size varied significantly from one sample to another. The 2D images were analyzed using VIZIO software; 3D imaging and animations of the inclusions were obtained by the region growing segmentation method. The tomography scan was conducted in the Zeiss Xradia 520 Versa; the sample cross section dimensions ranged from 600 µm by 600 µm to 3 mm by 3 mm with a height range of 10-45 mm. The Struers accutom-50 was used to perform a coarse cut of the samples. Finer dimensioning of the samples was achieved in an additional grinding step, this was performed by mounting the sample with

Quickstick 135 mounting wax on an adjustable metallic holder as shown in Figure 13,where the excess material could then be grinded away.

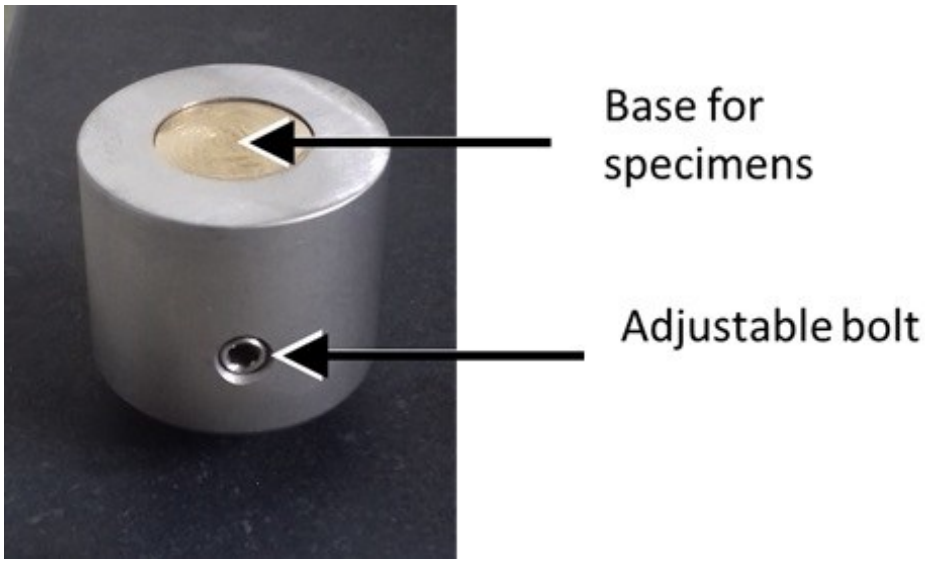

Figure 13 Adjustable sample holder

The raw data from the experiments comes in the form of image sets once the tomography scan has been performed, the data processing and acquisition software Scan-and-Scout makes an automatic reconstruction from the raw data as show in the workflow based on the Xradia Versa user's guide in Figure 14.

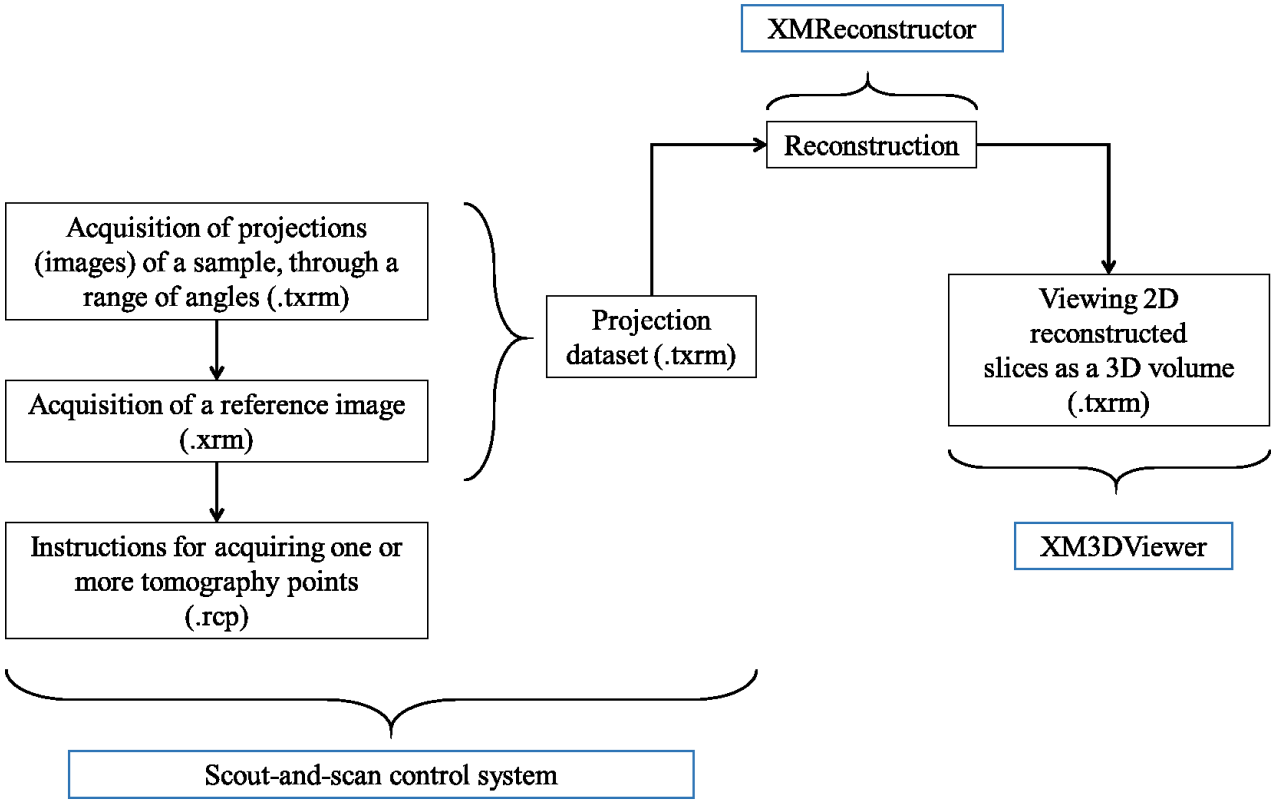

Figure 14 Data acquisition and processing for raw data

For the case of multiple scans, it is necessary to correct some parameters of the automatic reconstruction; in specific, the beam hardening, rotation, and center shift values, this will allow a whole reconstruction using the Manual Stitcher software and further manipulation can be done in Avizo where the user will be able to visualize the results as a single scan. The resulting data sets from this procedure tend to be large so a reduction on the voxel size is recommended using the "resample" function in Avizo. The shape of the voxel at this stage can be transformed from a cube to a cuboid, so a reduction on the number of images can be done in any of the three-dimensional Cartesian coordinate system of the sample (x, y, z). Even for the case of working with a single tomography dataset these settings needed to be adjusted, especially for the case of center shift as the given value can be manually improved resulting in better contrast on the images. The rotation of the sample was also a frequent issue and the surfaces of the sample needed to be aligned in the reconstruction stage. The resulting histogram of the 2D images include two peaks, the one with the lowest values corresponds to the surrounding air, while the second with a higher range corresponds to the metal sample, so the lowest peak needs to be removed. This can be performed with the "arithmetic" function where the values containing unnecessary information (noise) is subtracted from the histogram range of the image and is normalized to its original maximum value as shown in the following formula;

$$Histogram\ range = (A - H_{min}) \left(\frac{H_{max}}{H_{max} - H_{min}}\right) \qquad \textbf{Eq. 6}$$

Where A is the range of the raw data histogram, H_{min} is the minimum value to achieve the desired contrast and remove noise, and H_{max} the new maximum value to achieve the desired contrast, although, the maximum value of the original histogram A was kept most of the times. This could also be accomplished with any image editing software, but it is recommendable to do it from Avizo as it can work with large image sets. The main advantage of obtaining all the 2-D acquired images with a new histogram is due to the ease of image visualization during the serial sectioning as it will be simpler to match the images obtained from OM.

4. Results

The following section will present the results obtained from the different experimental set-ups and it will be divided in 5 sections corresponding to the different type of bearing that was analyzed. Some of the samples were ideal for multiple experimental methods while others presented various constraints that made them non-optimal for further investigation. The following activities were personally done, sample preparation for all experiments (cutting, polishing, grinding, mounting, OPS, etching); collection of results and operation of optical microscopy, scanning electron microscope, serial sectioning and EDS; finally, data analysis (segmentation and reconstruction of some results). Extensive help was received by Søren Fæster for tomography scans, Chuanshi Hong for EBSD and Gitte Christiansen for epoxy and nital preparation.

4.1. Wind turbine radial ball bearing

The investigation of this sample was extensive as it presented various visible butterfly-cracks with clear indication of WEAs; Figure 15 is shown as an overview of the extensive damage in the bearing, the black stains that appear to be inclusions are localized etching, the yellow arrow indicates assumed rolling direction based on literature for all images. Figure 16 is presented as a close-up to the regions of interest showing WECs. The images are oriented as to show the raceway on top, the revealed cross section is normal to the rolling of the bearings. Since the bearing was obtained from a wind turbine no information was provided regarding exact operational conditions.

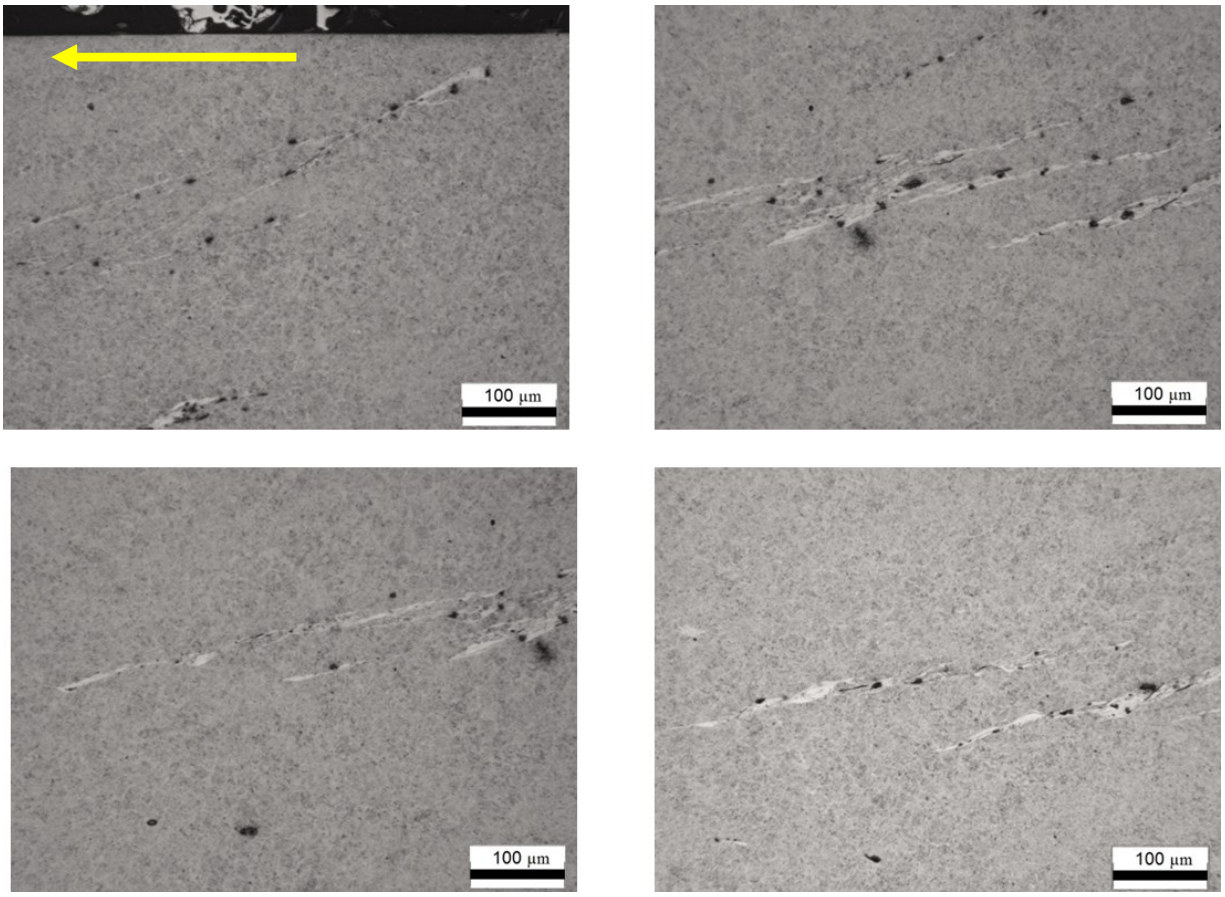

Figure 15 Overview of butterfly cracks in WT radial ball bearing

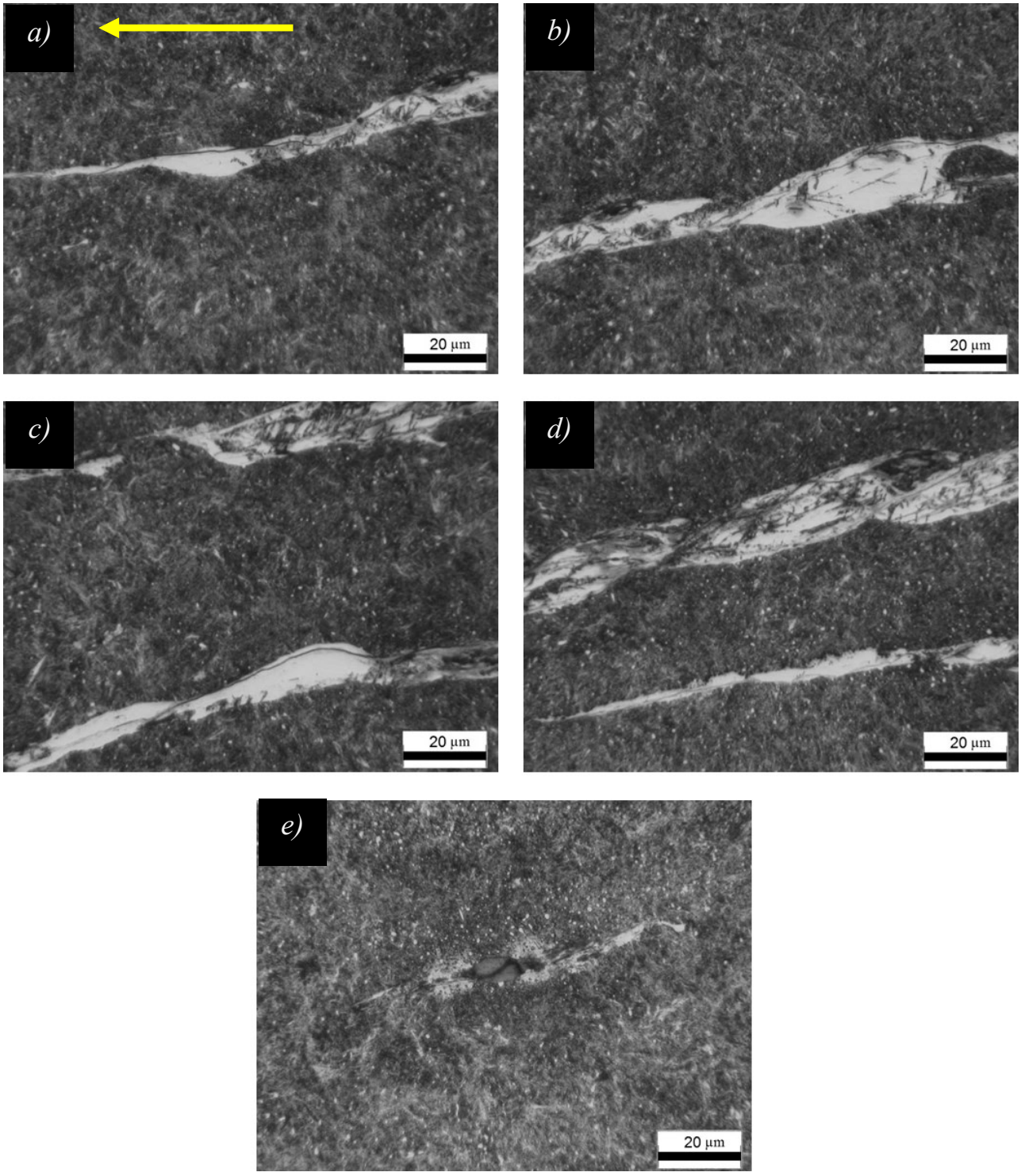

Figure 16 Close-up to regions of interest from Figure 15

Figure 16 e) is of interest as it shows an inclusion with a crack going through it and a WEA around the crack. The black dots are the result of an aggressive etching, indicating a possible DER. A region with several cracks was chosen from the sample to perform a tomography scan as shown in Figure 17 where the yellow arrow shows the possible rolling direction and results are presented in Figure 18.

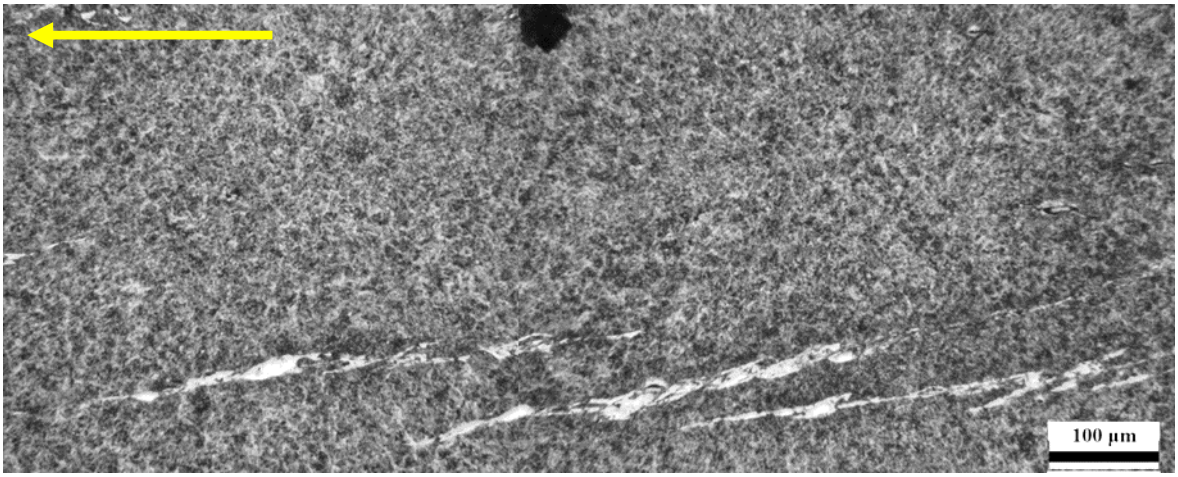

Figure 17 Region of interest for tomography scan.

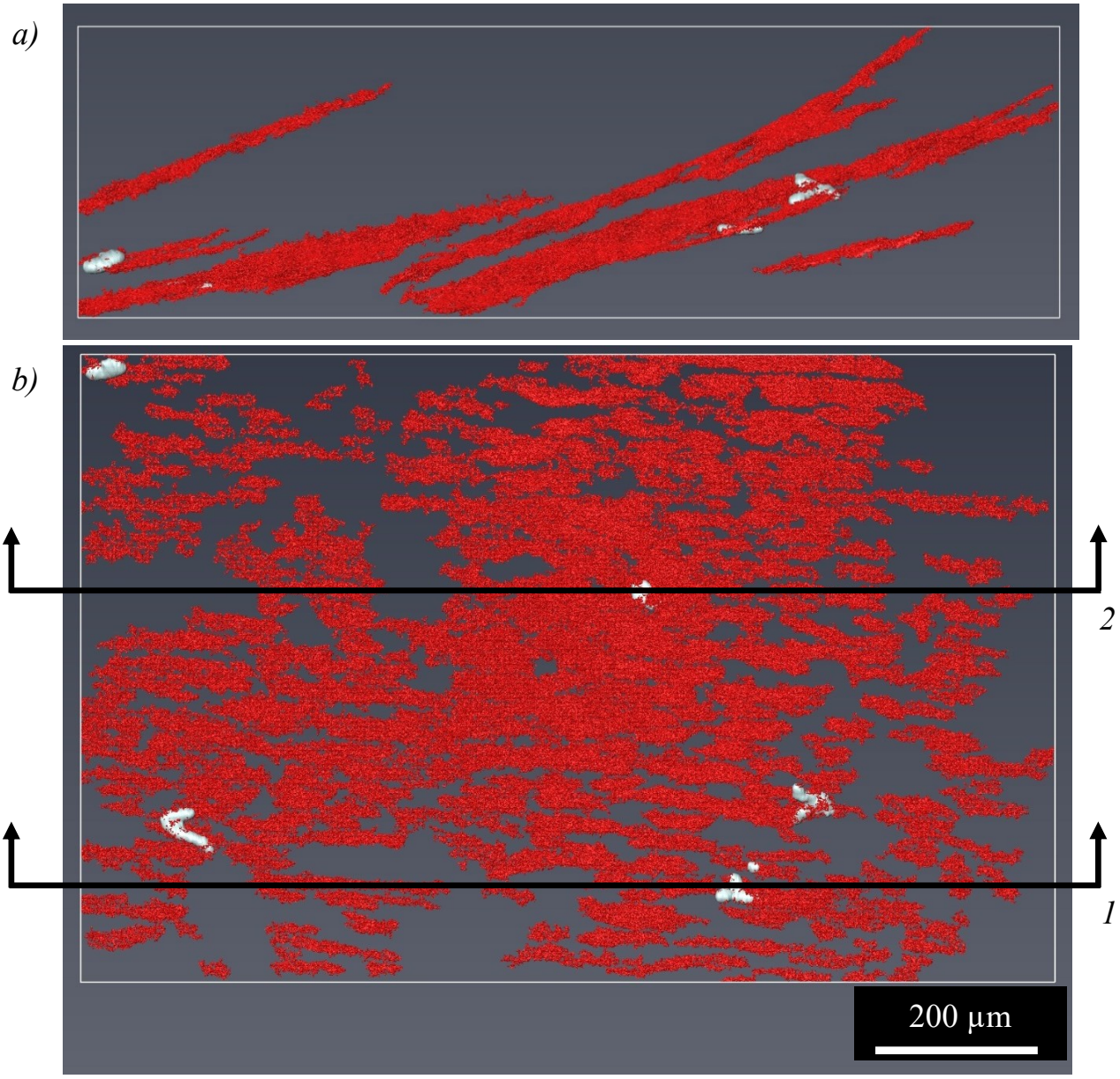

Figure 18 3D Tomography scan results from Figure 17, front view (*a*) and top view (*b*), inclusions-like regions and cracks are colored white and red respectively

Figure 18 *a*) shows the same view as presented in Figure 17 while Figure 18 *b*) shows the sample viewed from the raceway perspective (top view). It is noticeable that the scan shows the butterfly cracks running parallel to each other, this was later confirmed by serial sectioning. The angles at which they are propagating are well within the range described by other authors, 30º to 50º. The inclusions interacting with the cracks were colored white and artificially enlarged as to make them visible by the region growing segmentation method. Although the segmentation method could not catch all the details of the butterfly cracks, it showed characteristics that otherwise could not be observable. More importantly the results were used to reveal the enlarged inclusions and four regions of interest were identified for serial sectioning. The first revealed surface by optical microscopy shows a remarkable similarity compared to the tomography scan, marked *(1)* in Figure 18, and in the future referred as surface *(1)*, the results are compared in Figure 19.

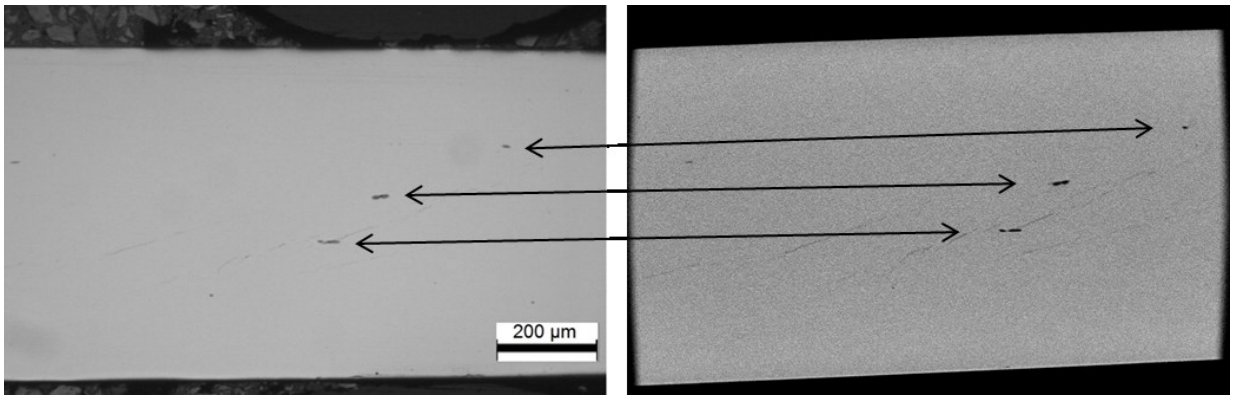

Figure 19 Comparison of OM (left) vs results from tomography scan of surface *(1)* (right)

Figure 20 shows two SEM images from surface *(1)* at different depths, where a change in the shape of the inclusion and crack is visible.

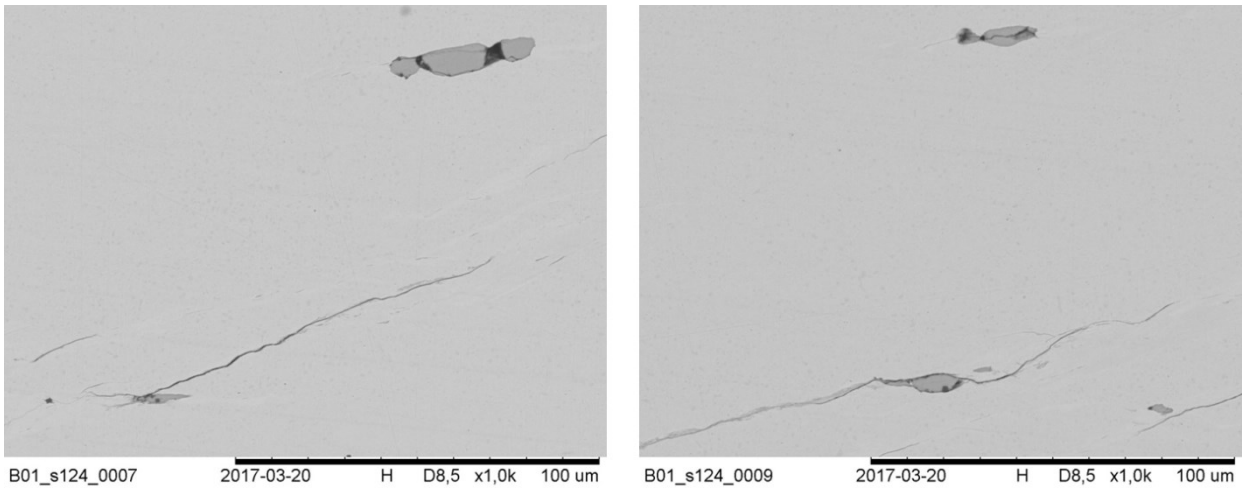

Figure 20 SEM results for revealed surface *(1)* as shown in Figure 19

Similarly, Figure 21 shows the second revealed surface as shown in Figure 18 *b*) and labeled as surface *(2)*.

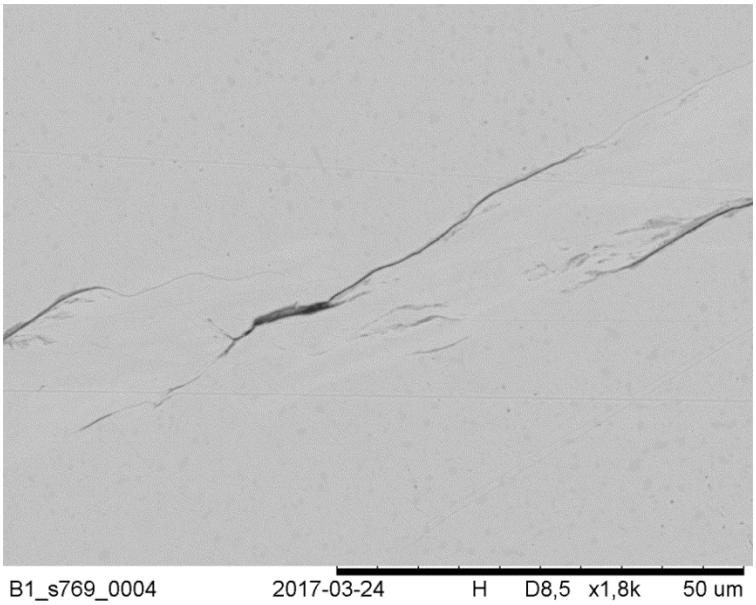

Figure 21 SEM results for revealed surface *(2)* as shown in Figure 18

The EDS results for surface *(1)* showed two elements, manganese and sulfur, suggesting a manganese sulfate inclusion, on the other hand, results of surface *(2)* showed a high carbon content, suggesting a graphite inclusion or sample contamination from the epoxy used, the EDS results are shown in Figure 22.

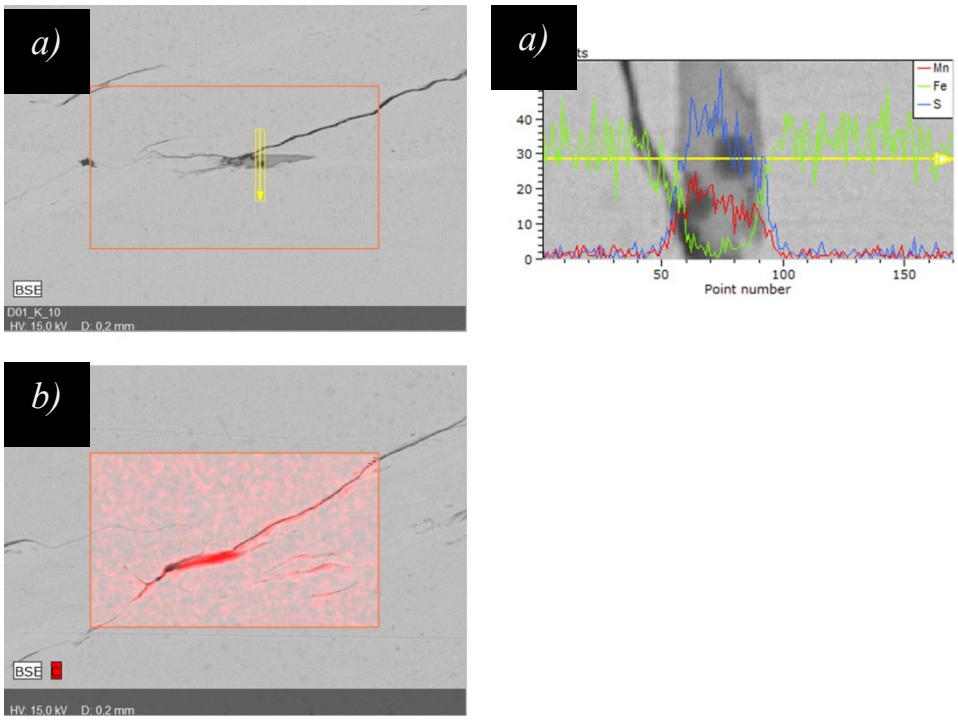

Figure 22 EDS results for surface *1 (a)* as shown in Figure 20; Mn (red), Fe (green) and S (blue). Results for surface *2 (b)* as shown in Figure 21; Carbon (red)

Although it was possible to map four areas of interest using tomography, some limitations were also observed during the experiments, as some inclusions with small cracks or cracks within were out of range from the equipment's resolution. Although the inclusions themselves were visible in the tomography scan, the cracks observed in the SEM were not captured in the segmentation process. Some examples are presented in Figure 23.

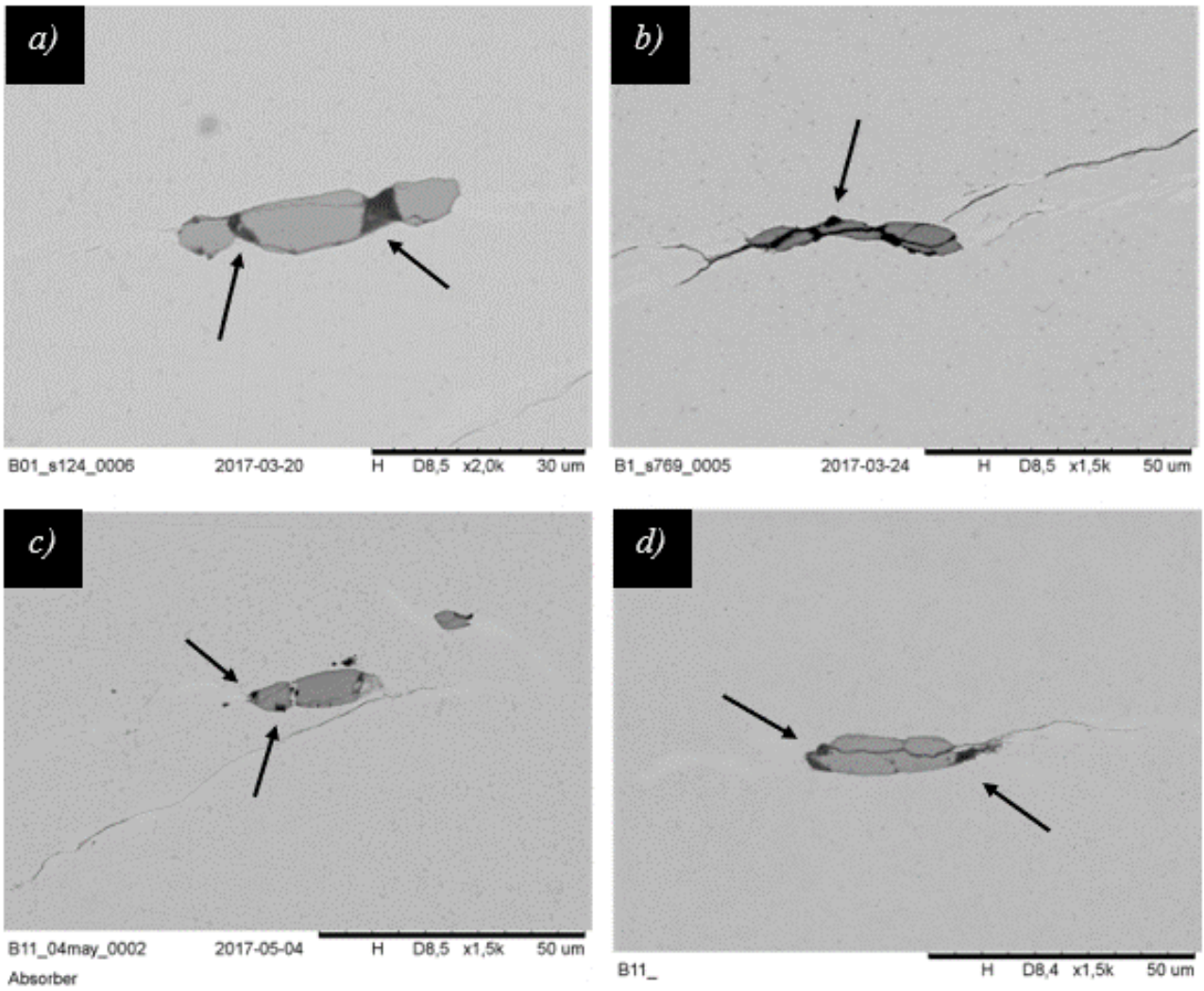

Figure 23 SEM results showing inclusions with inner cracks

EDS experimentation was performed to results in Figure 23, all of them were manganese sulfates nevertheless, sample *a*) showed the presence of carbon, pointed by the arrows, while samples *b)*, *c)* and *d)* showed the presence of aluminum oxide, pointed by the arrows. Except for sample *b)*, the inclusions were isolated from the main butterfly cracks. Although four regions were identified by the tomography scan with cracks-inclusions interactions, only two could be investigated. The main factors for this were near proximity between regions (<80 µm), which resulted in over-polishing while trying to reveal one of the surfaces, also, limitations for samples with a thickens of less than 50 µm, as the material falls from the holder resembling a metal foil.

4.2. Axial bearing

The sample was tested in a FE8 test rig in RWTH Aachen University, Germany with the following operational conditions: axial load: 80 kN (max. contact force), rotational shaft speed: 300 RPM, bearing mass temperature: 100°C, oil flow rate 0.25 l/min and an averaged specific film thickness ratio of: 0.59 [35]. The sample was cut to observe the most damaged region according to an ultrasonic measurement as seen in Figure 24, this experiment was not conducted during this research and results are just shown.

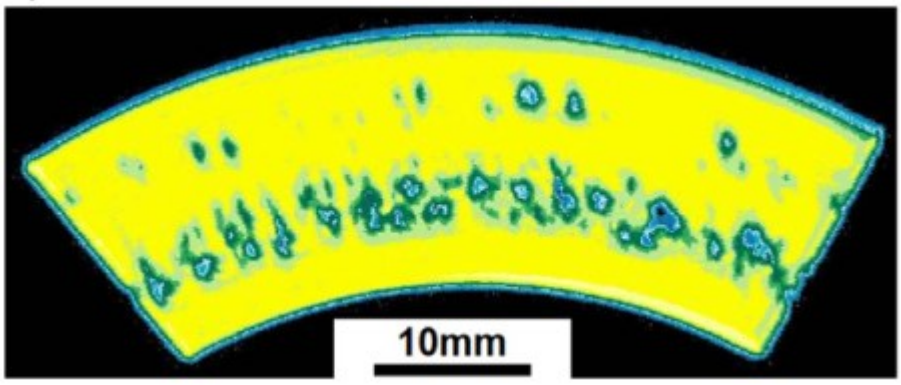

Figure 24 Ultrasonic results showing the most damaged area of the raceway [35]

It was found that the sub-surface was heavily damaged and a crack network was visible, in some regions of the raceway the cracks already had reached the raceway surface and the width of the cracks were considerably large as shown in Figure 25, where the yellow arrows indicates the rolling direction.

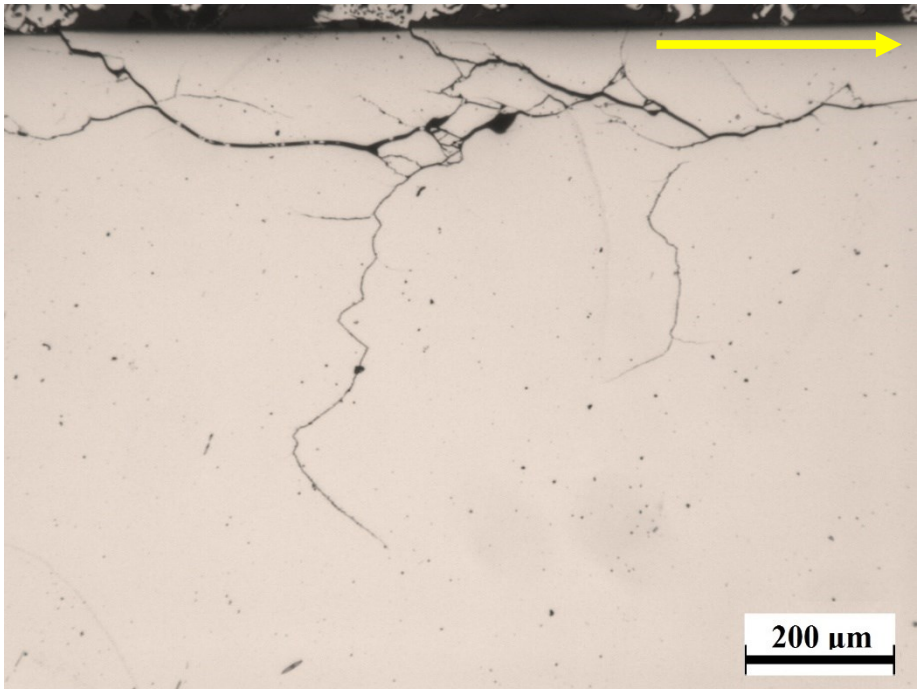

Figure 25 Region from axial bearing with extensive damage, sample obtained from bearing shown in Figure 24

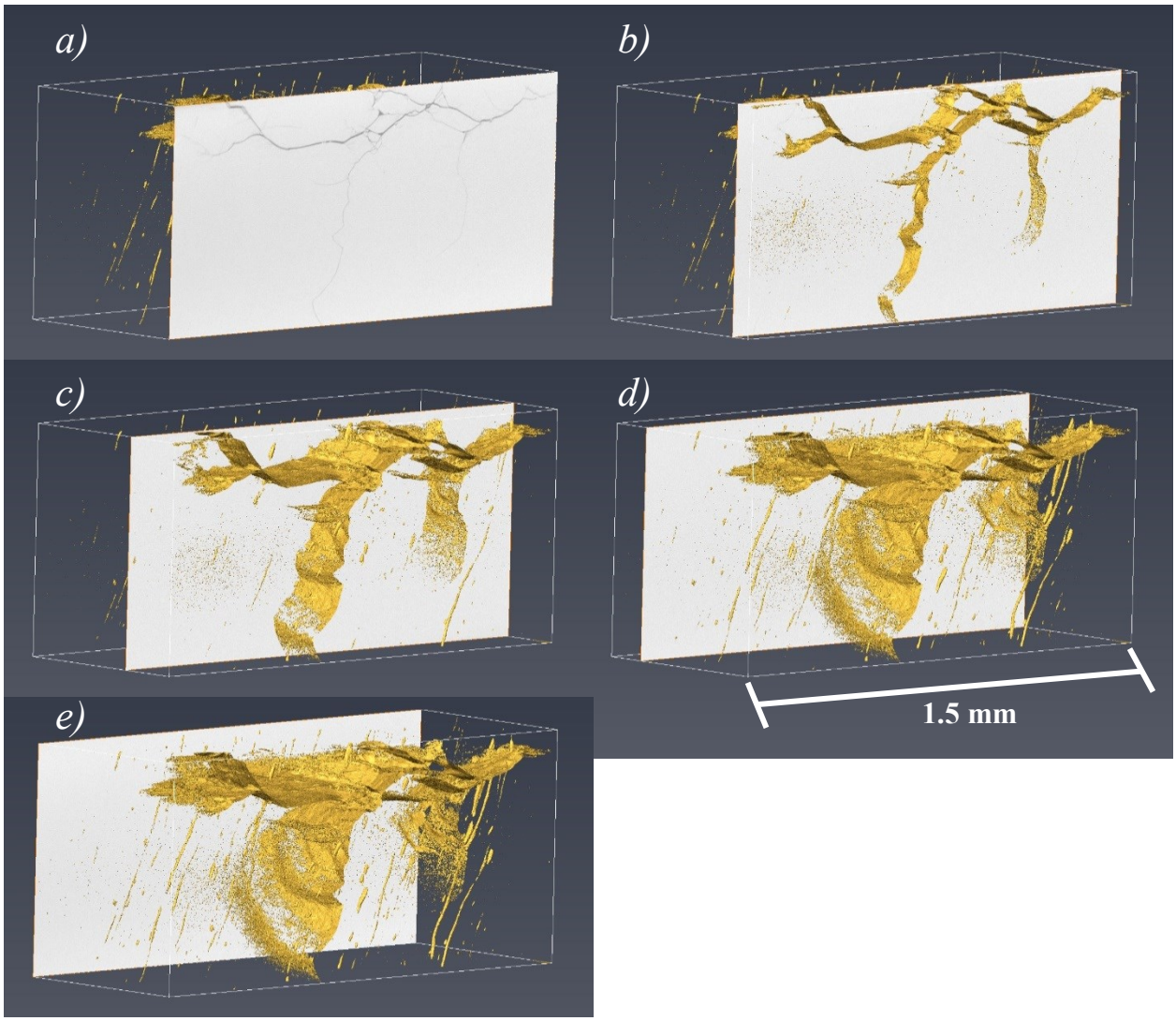

Figure 26 Post processing of raw data and crack-inclusion mapping, results are from sample in Figure 25

Figure 26 shows the tomography results and how it mapped the crack; due to the crack width, it was possible to obtain a remarkable 3D reconstruction. The results were processed using the automated "Isosurface" command on Avizo. The inclusions are shown as elongated entities, nevertheless due to the heavy damage in the region the interaction between inclusions and cracks could not be observed in detail and no significant conclusion could be reached in this matter. A second sample was cut to observe a triple junction of the crack to investigate the propagation direction and whether grain boundaries have any influence on its path. The analyzed region is shown in Figure 27 where the yellow arrow indicates the rolling direction. The results of the EBSD is shown in Figure 28 which was conducted with a step size of 0.05 µm.

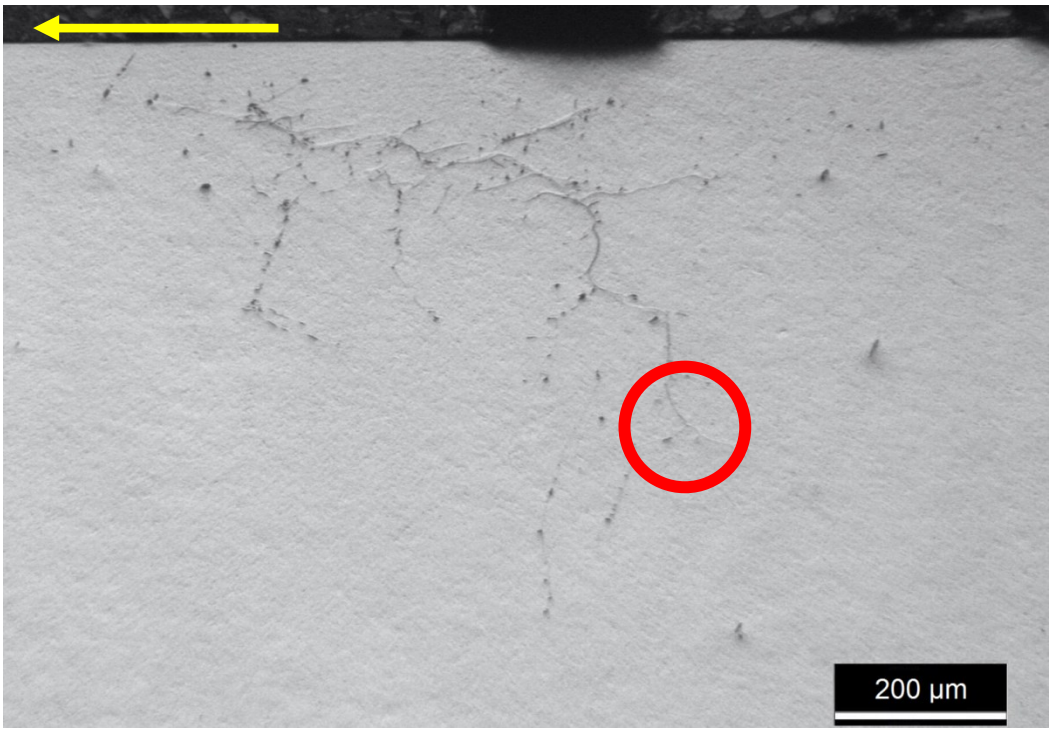

Figure 27 Triple junction of crack and region of interest for EBSD

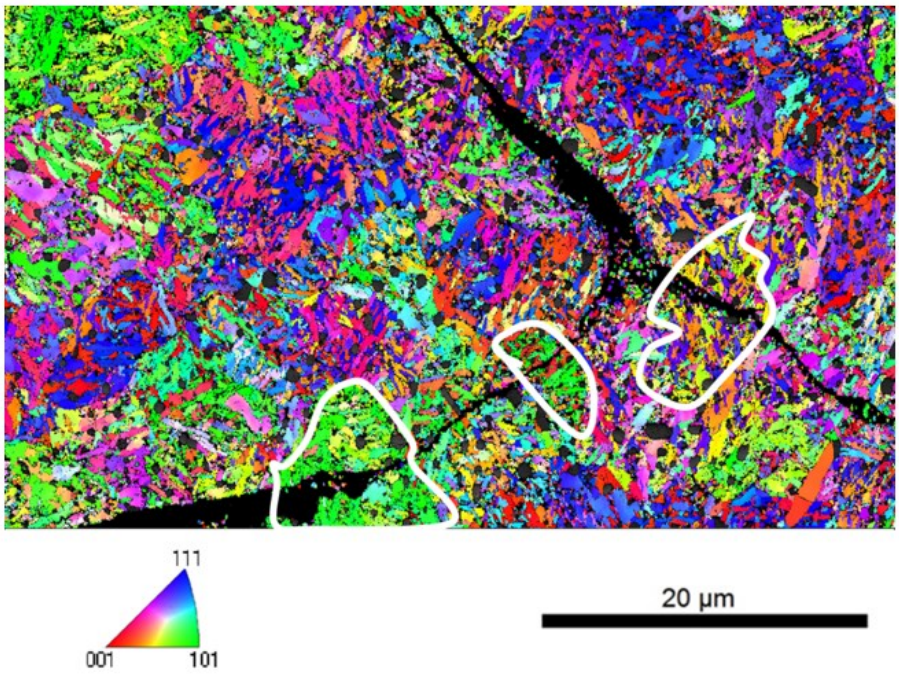

Figure 28 EBSD results from region highlighted in red in Figure 27 (iron BCC matrix)

As it can be observed from Figure 27 the width of the crack network is thinner compared to the one presented in Figure 25, nevertheless the cracks are already approaching the surface and propagating inside the material. The EBSD study demonstrates that the crack is propagating through prior austenite grain boundary (PAGB) highlighted by a white contour. A reduction in grain size is observed near the cracks or in the WEAs, these regions are colored in black in Figure 28 and are undistinguishable from the crack. Both regions cannot be indexed due to the

absence of a micro-structure. Cementite particles can also be observed and are colored in dark grey.

For the serial sectioning a sample was obtained and it was previously studied in [35]. This sample had already been scanned under the tomography, but the raw data needed to be processed to achieve the desired contrast and ease in the matching of images obtained from the OM. In the tomography results it can be observed some interaction between the cracks and voids or inclusion-like particles, as seen in Figure 29 and highlighted by the arrows, yellow arrow indicates rolling direction.

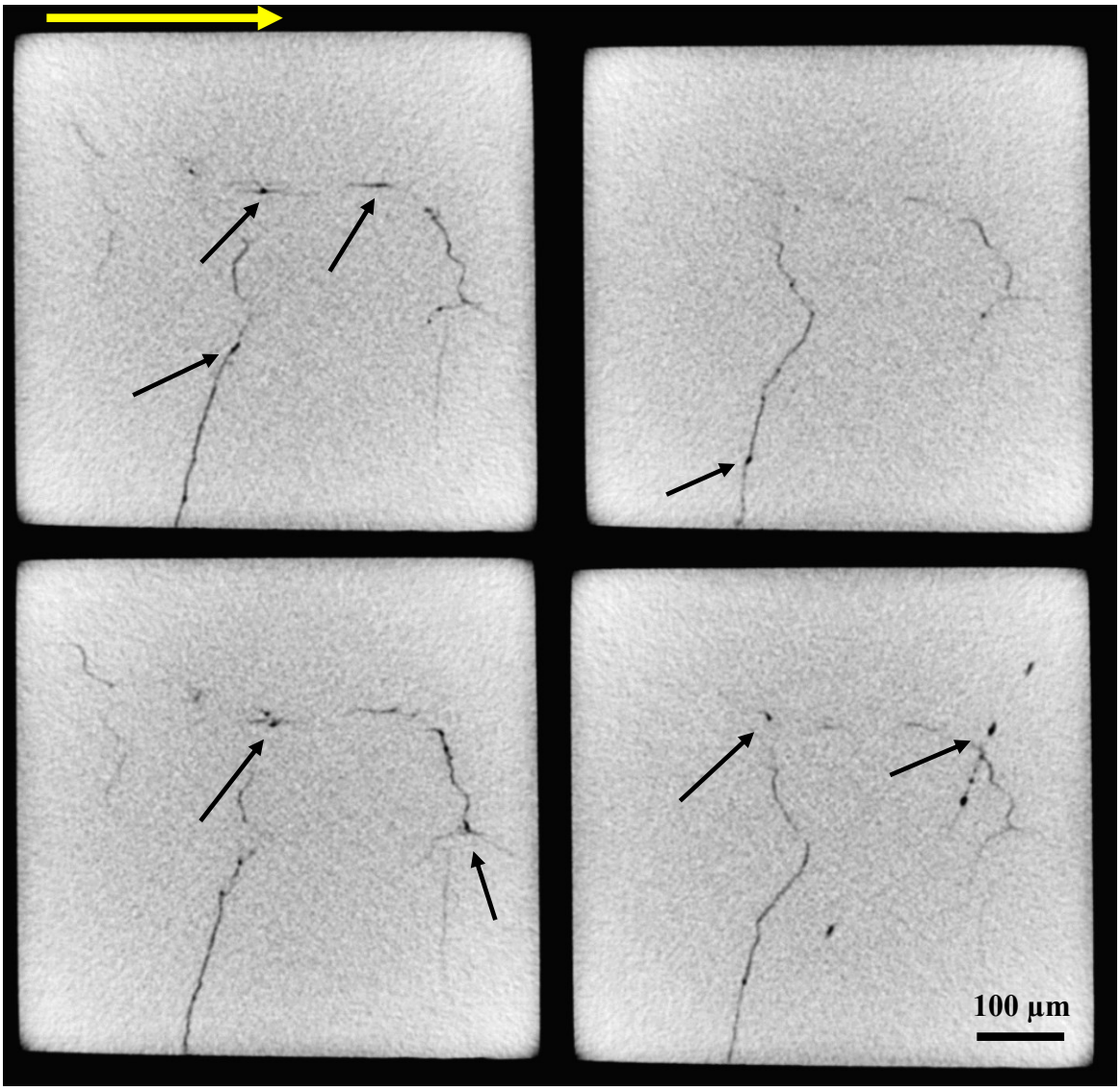

Figure 29 Tomography scan results from an axial bearing tested in a FE8 test rig

The obtained sample was already cut and mounted for a serial sectioning study, nevertheless, there was a gap between the steel and the surrounding resin which lead to ethanol intake and would later resurface in the vacuum chamber of the SEM. The sample needed to be unmounted, a delicate process due to the sample dimensions (560 µm × 600 µm × 1400µm) and remounted using a steel holder on a Condufast matrix. Once the sample was mounted, grinding and

polishing was performed in steps of 50-100 µm until a tomographic scan was matched to the revealed surface. While performing this process it was of importance to look for unique features in both the revealed surface and the tomographic scan, as shown in Figure 30.

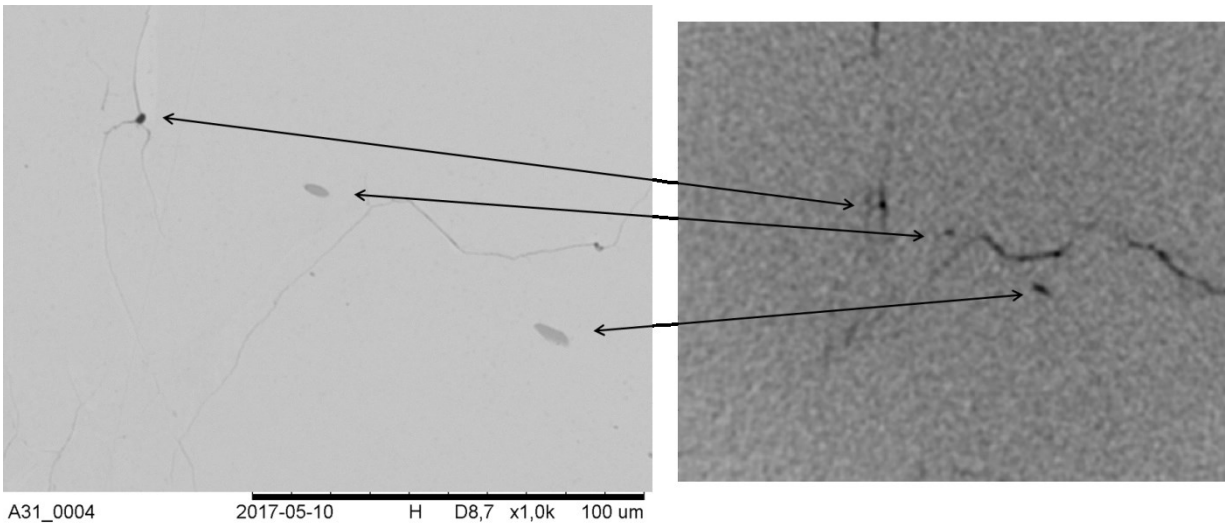

Figure 30 Comparison between SEM image (left) and tomography scan (right)

Although it is not an exact match, three inclusions are seen in both images, the discrepancy might be due to the tilting of the sample while pressed in the mounting process. So, the orientation of the physical sample and the data will not match exactly, still the same features can be observed and it was possible to distinguish the position of the cross section and was confirmed by other unique features observed above and below the encounter of this cross section. Once the sample surface was matched with the tomography scan it was not necessary to measure the depth of the polish via a hardness indent or a micrometer. The voxel size of the data set, 0.48 µm for this case, will indicate the depth of future polishing stages and thus reducing the time of the serial sectioning process. Of special interest is the chemical composition of the inclusions observed on the crack and highlighted in a red circle in Figure 30 showing a triple junction and an inclusion-like feature in the middle. The EDS results showed the presence of carbon as shown in Figure 31.

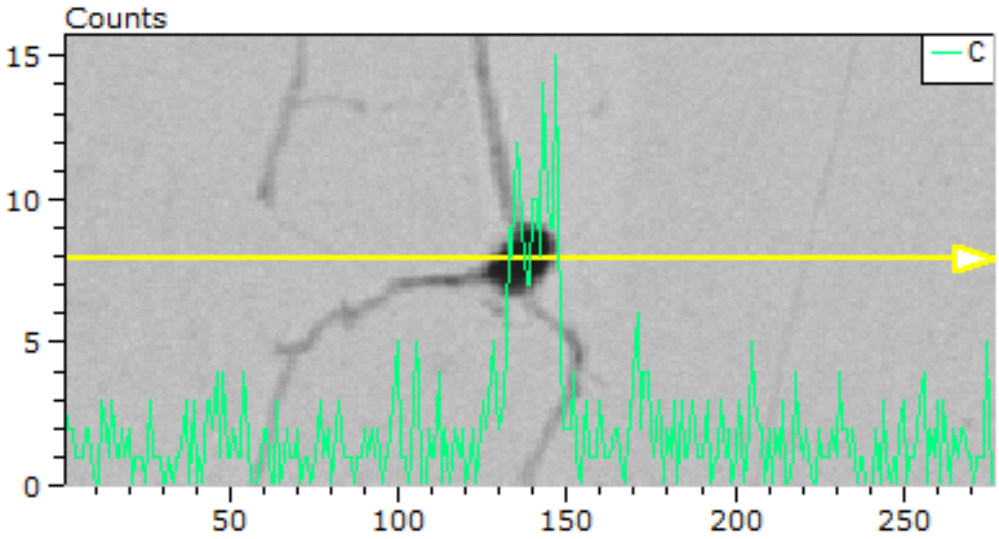

Figure 31 Carbon results in EDS experiment from triple junction crack shown in Figure 30

It thus can be concluded that the inclusion in this region is either graphite or sample contamination from the holder and due to time constraints only one surface was investigated, but the tomography scan showed various regions with similar interactions between cracks and inclusion-like particles. Overall, less damage was observed in the outer contact surface between the raceway and the roller as predicted by [35] and shown in Figure 24. Although only one triple junction was observed under the EBSD as seen in Figure 28, it was possible to conclude that the crack propagated over what seems to be a PAGB.

4.3. Wind turbine main bearing

This sample was obtained from a WT main bearing, since it experienced infield conditions no information on operational information was given by the supplier, however due to the crack size and inclination it was not an optimal specimen for a tomography scan, an overview of the crack is presented in Figure 34, although not shown, the raceway is located approximately 1.7 mm away from the inclusion highlighted in red as shown in Figure 34. When observed under the SEM it presented two regions of interest, both with a triple junction, but one of them revealed a large inclusion *(b)* as shown in Figure 32.

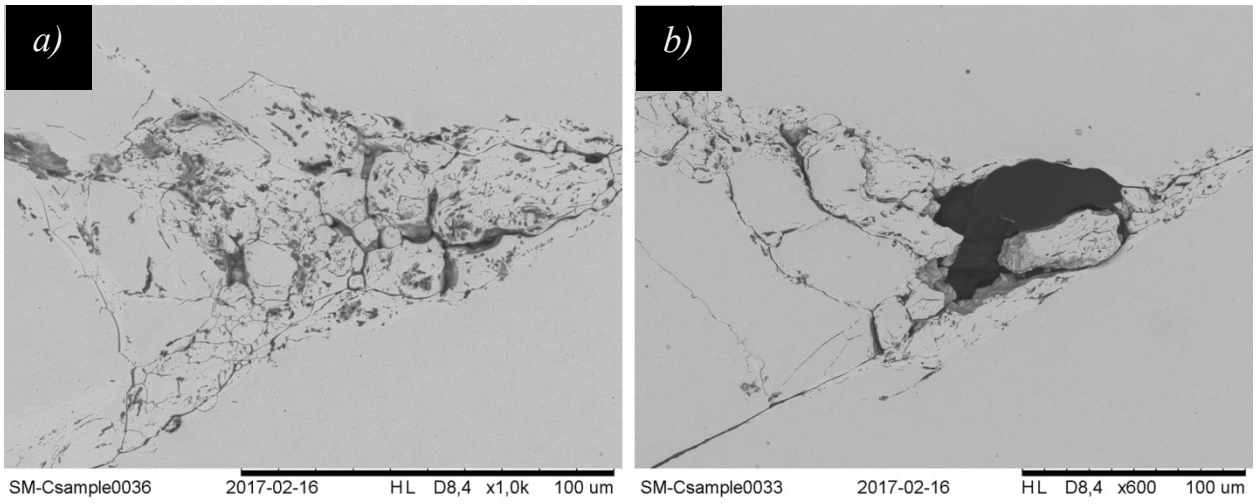

Figure 32 Regions of interest in WT main bearing regions *a*) and *b)* are highlighted by a black and red circle respectively in Figure 34

The pattern on the crack shown in Figure 32 *a)* might had been an indication that the crack was extending along prior austenite grain boundaries, thus an EBSD test was conducted with a step size of 0.05 µm, however no significant results were obtained due to heavy plastic deformations and a considerable decrease in grain size as shown in Figure 33.

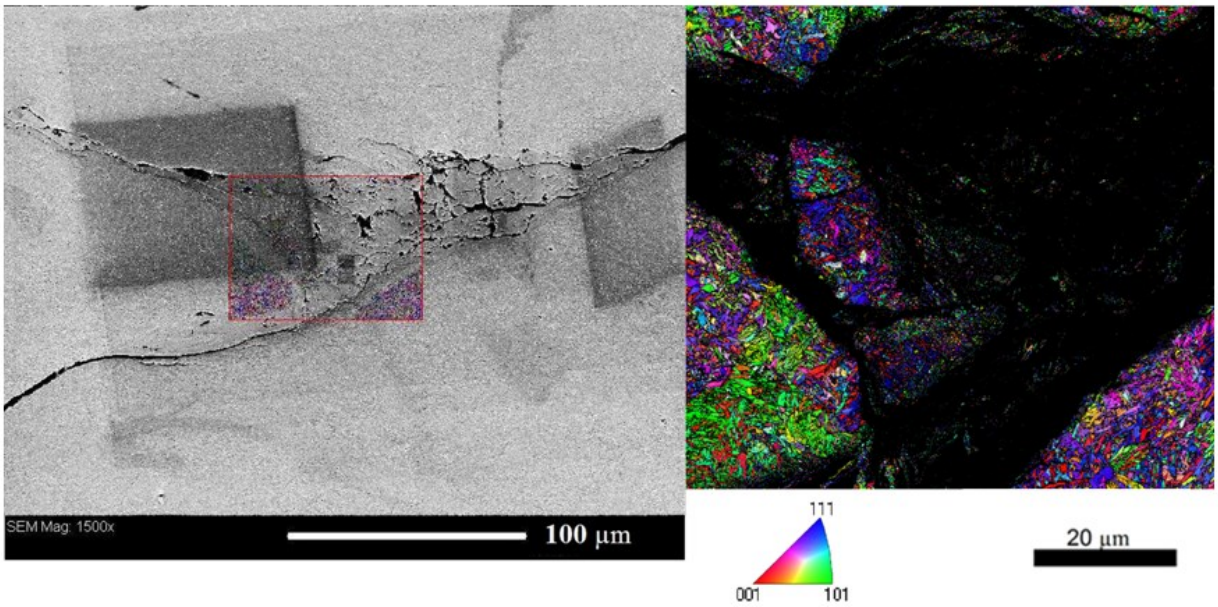

Figure 33 Overlay of EBSD results on top of a SEM image (left) and EBSD results corresponding to an iron BCC matrix (right) region shown in Figure 32 *a)*

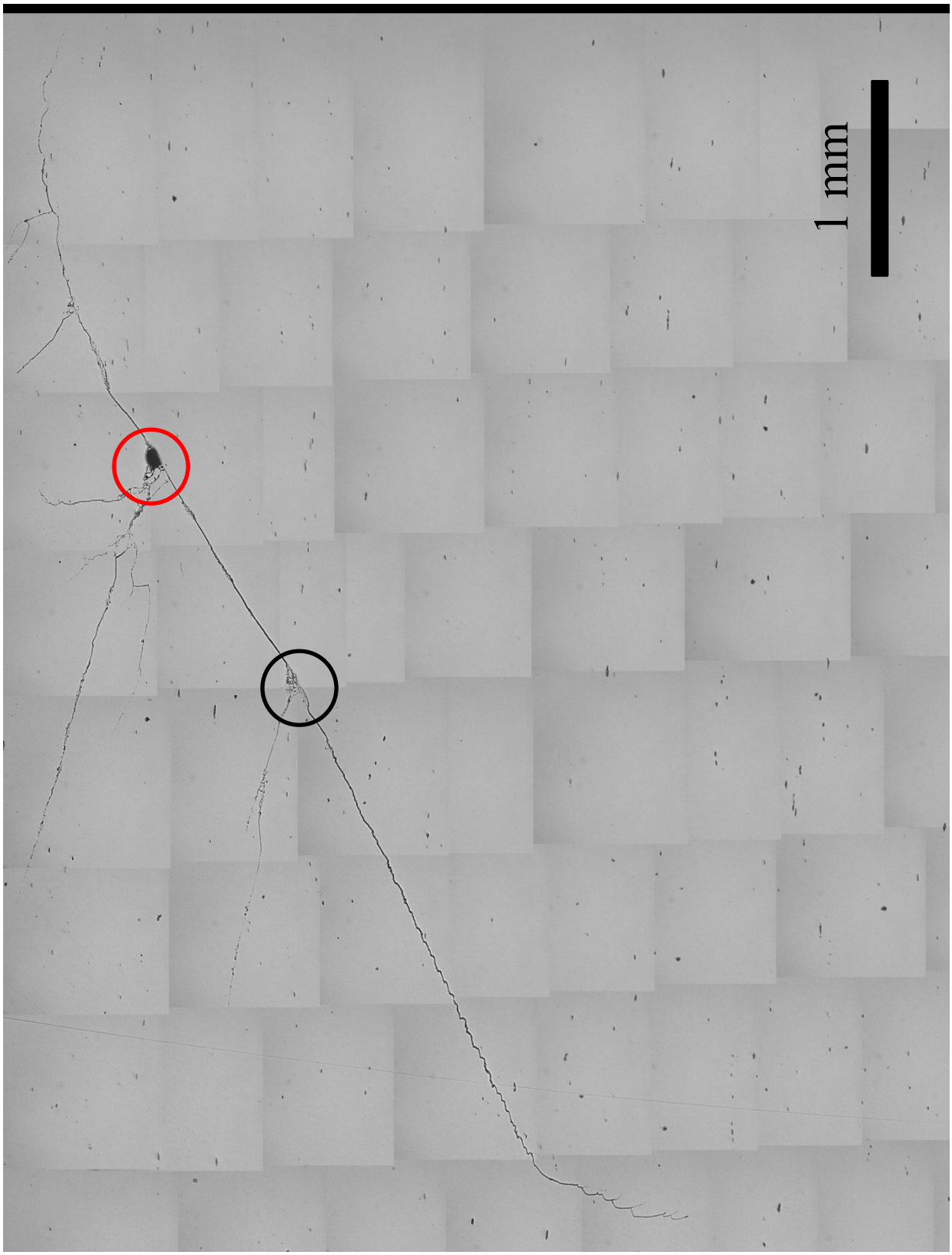

Figure 34 Overview of crack on main bearing

4.4. Radial bearing from test rig

A sample was extracted from a radial bearing that was previously tested under controlled conditions in a test rig. The sample was provided from a bearing manufacturer and no further information was supplied. A crack was observed going through one inclusion (top black arrow) and another one very close to it (bottom black arrow) as shown in Figure 35, the yellow arrow indicates assumed rolling direction based on literature, the top of the crack is located at approximately 150 µm away from the surface.

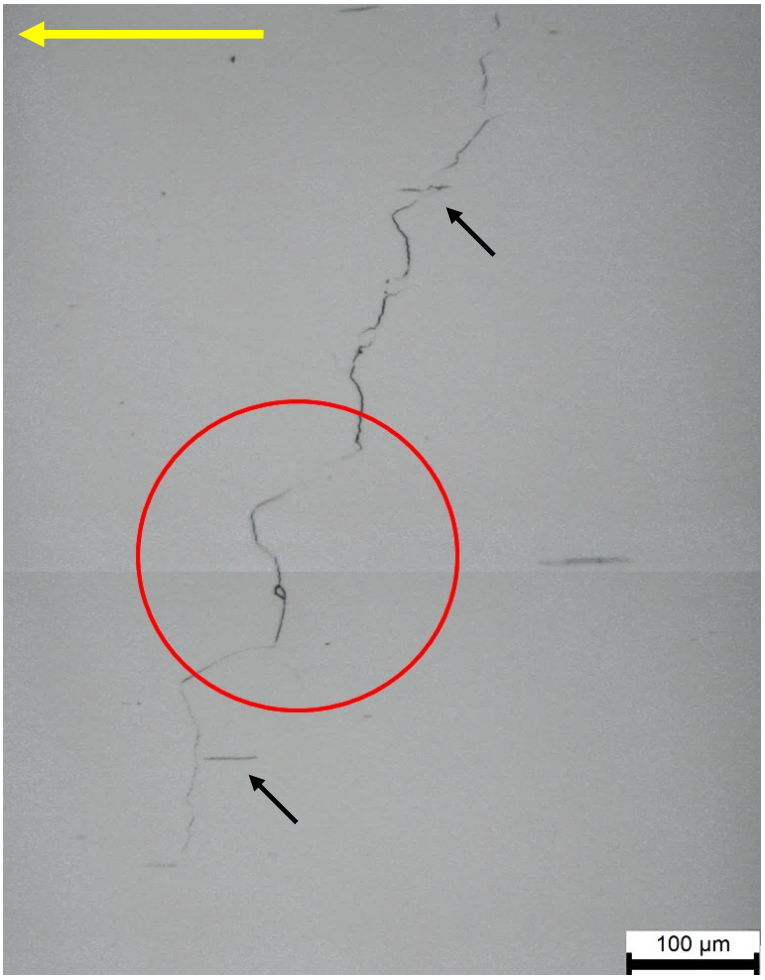

Figure 35 Crack from radial bearing under test rig

After being etched some WECs were observed especially in the region enclosed by the red circle in Figure 35 and shown in Figure 36.

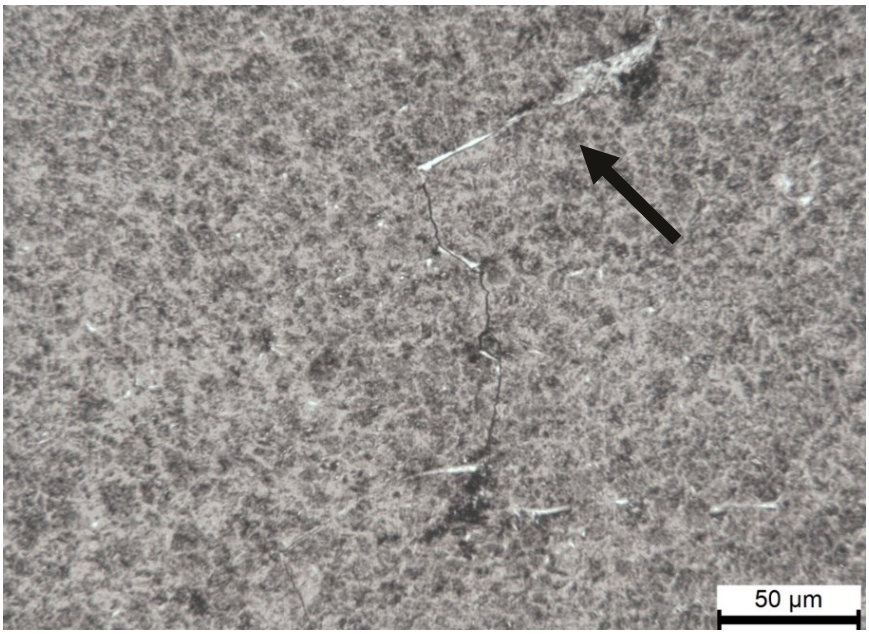

Figure 36 White etching cracks in radial bearing indicated by arrow, close-up from Figure 35

As the final step for this investigation a tomography scan was performed, and the results are shown in Figure 37 where the cracks and inclusions are colored in grey and pink respectively. The results captured the inclusions seen on the surface of Figure 35 and although the bottom inclusion seemed to be separated from the crack, the scan showed there was an interaction between them at a different depth.

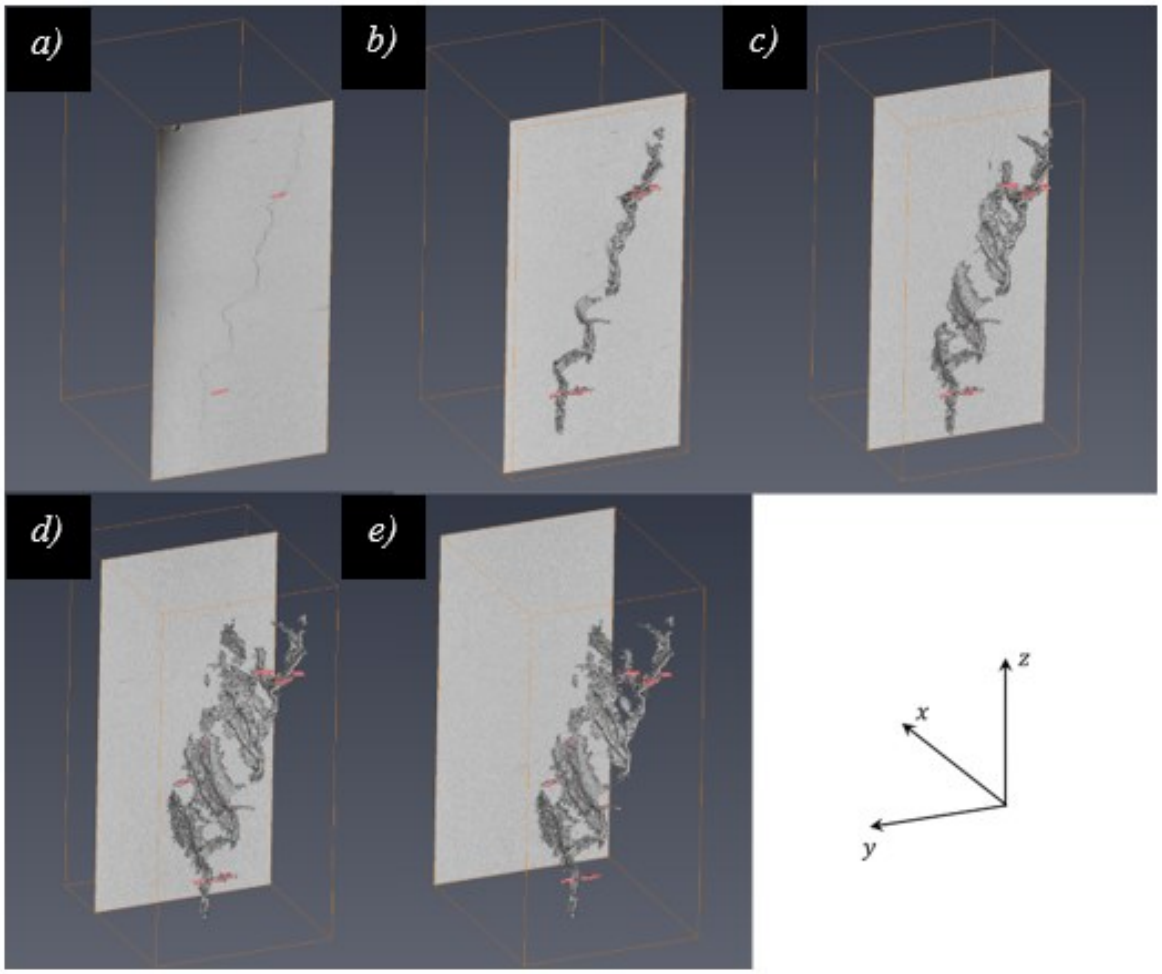

Figure 37 Tomography scan results from sample shown in Figure 35
Physical dimensions of scan are $x = 450\mu m$, $y = 85\mu m$, $z = 470\mu m$

4.5. Wind turbine tapered bearing

The specimen was obtained from a tapered bearing and underwent unknown operational conditions in a wind turbine. The cracks were visible from the surface and were perpendicular to the rolling direction. The specimen for the tomography was the largest during these experiments with cross-sectional dimensions of 3mm by 3mm and a height of 45mm; the scan of the sample was divided into 7 parts. The raw data was then overlapped and combined into a single file by the Manual Stitcher software; the final file was resampled to facilitate its analysis by increasing the voxel size from 3.5 µm to 8.5 µm, thus reducing the quality of the scan but also decreasing the size of the file. The results of the tomography scan are presented in Figure 38.

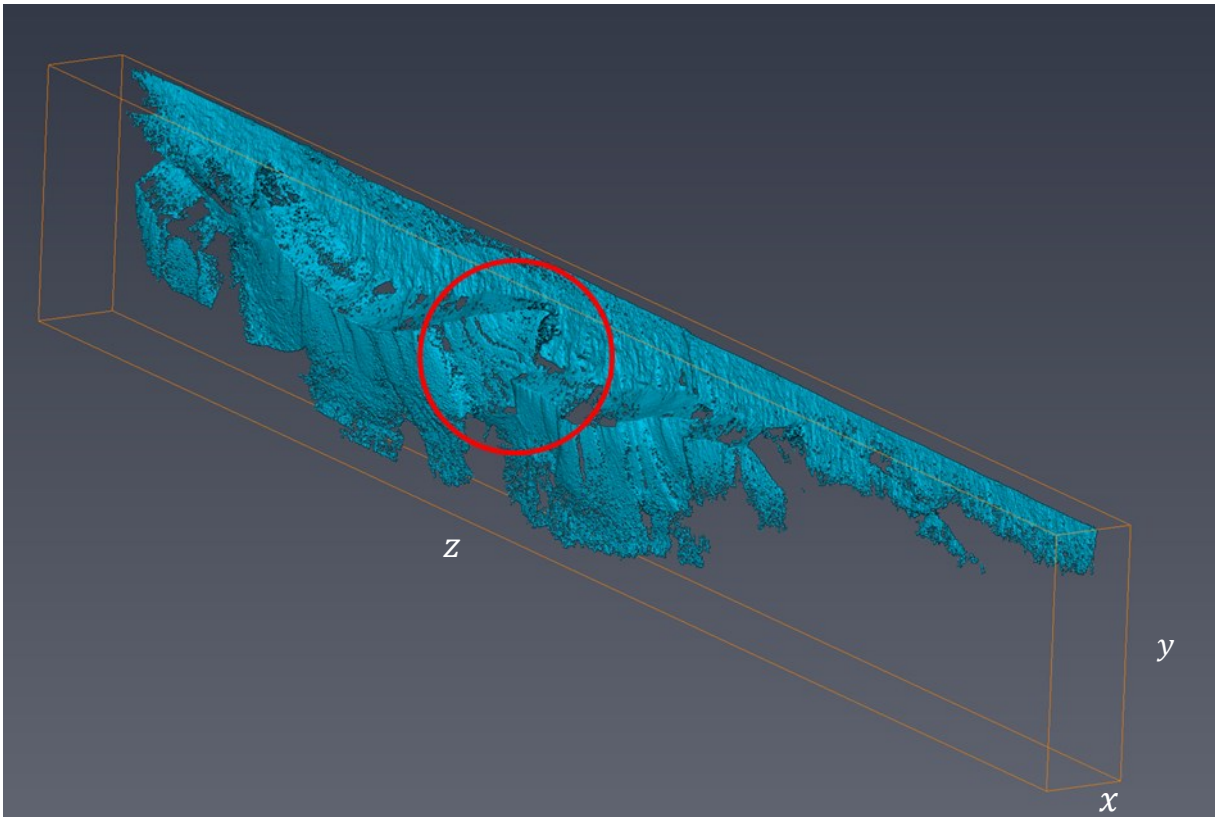

Figure 38 Tomography scan of wind turbine tapered bearing
Physical dimensions of scan are $x = 1.51mm$, $y = 4.50mm$, $z = 32.87mm$

Of interest is the region enclosed by the red circle in Figure 38, where two cracks interact, the cross-sectional results obtained from the tomography scan are presented in Figure 39, the arrows indicate particles or voids interacting with the crack.

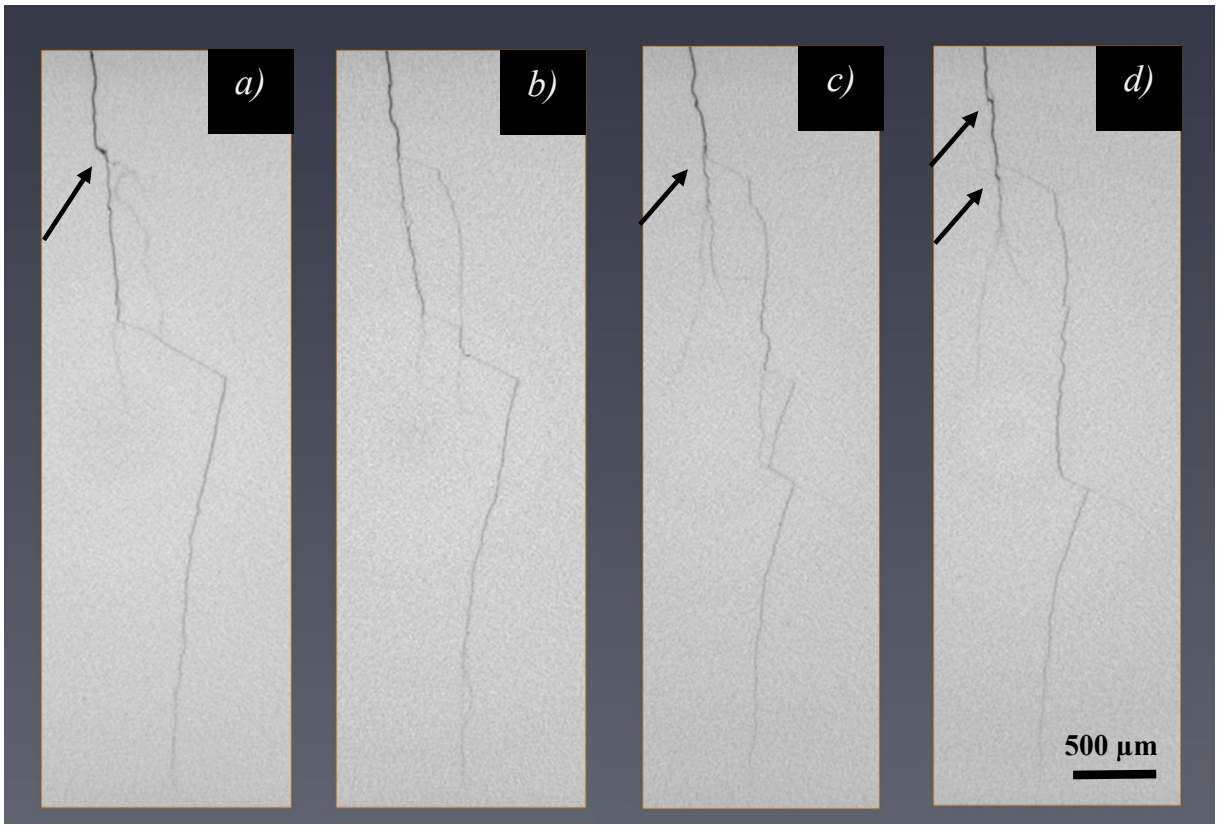

Figure 39 Results of tomography scan showing the interaction between cracks, images were obtained from encircled area of Figure 38

It can be observed that a small crack is formed in Figure 39 *a)*, a particle is observed and pointed by the arrow. The crack seems to grow erratically but starts to grow perpendicularly to the main crack as shown in Figure 39 *b)* creating a step-like shape. The crack continues to grow downwards and the step like shape is lost as seen in Figure 39 c*)*. Finally, it merges as a single crack and will continue to have this shape along the specimen as shown in Figure 39 *d)*. A close-up of the crack in 3D is shown in Figure 40, the cross-sectional images from Figure 39 were obtained from this volume and the step-like shape is highlighted in red. Following the edges of the cracks it can be observed they have a slight curvature and these features are highlighted in yellow in Figure 40.

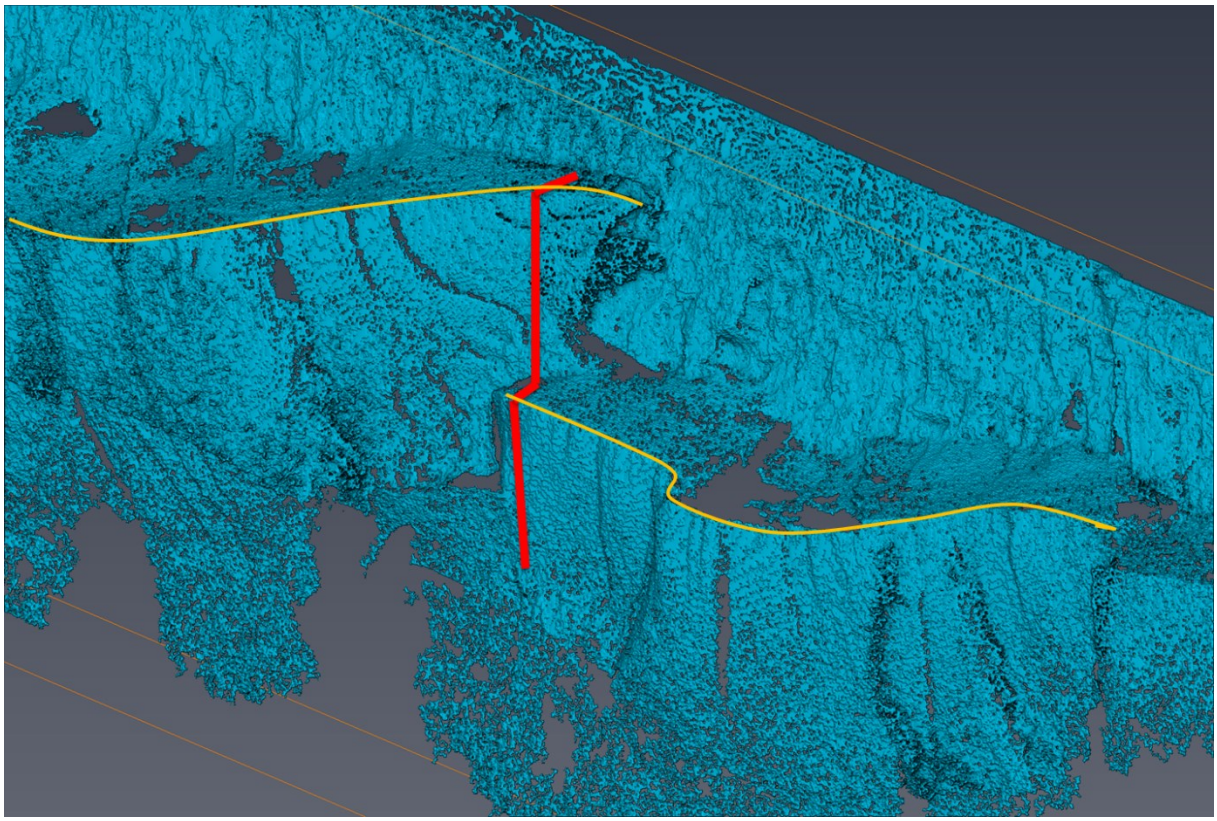

Figure 40 Interaction between cracks, a close-up of enclosed region showed in Figure 38. Red line is the contour of cross-section shown in Figure 39 *b)*

5. Conclusions

The presented method using 3D X-ray microscopy successfully mapped various cracks and inclusions giving the possibility of further investigation by serial sectioning. The main advantage of this method is the time saved in data acquisition when compared to other methods such as optical microscopy or SEM, although some limitations were observed in the 3D reconstruction of inclusions with inner or finer cracks. The segmentation method in Avizo was able to make 3D reconstructions of various types of cracks, from simple straight cracks to complex networks. The cross-sectional tomography results in 2D when compared to optical microscopy images were very similar, giving a good overview of the crack and inclusions but not able to capture finer details. Alternatively, SEM images captured finer details in both cracks and inclusions alike, outperforming the results obtained from the tomography scan. Results showed most cracks located at the sub-surface of the raceway, which is consistent with rolling contact fatigue and concentration of von Mises stresses at the sub-surface. Although two samples presented cracks at the surface, it was not possible to determine the location of the crack initiation. Despite readings of high carbon content in the EDS results, it was not possible to conclude the presence of graphite inclusions due to possible contamination of the carbon base epoxy from the sample mount.

The results in section 4.1 showed that the cracks initiated in the subsurface most probably at inclusions, creating the so-called butterfly cracks. Of interest is to note that the EDS results showed that the inclusions with the presence of manganese sulfate and aluminum oxide did not propagate as much compared to manganese sulfate inclusions. In section 4.2 sub-surface initiation was also observed, however, some regions of the bearing presented cracks that reached the surface. This resembles the type of initiation suggested in [8] where due to a successive accumulation of distortion at cementite particles suddenly transforms into a WEA and cracks. This theory would explain the crack propagation in prior austenite grain boundaries (PAGB) as revealed in the EBSD results and the complex crack network. The specimen of section 4.3 was too large for a tomography investigation but presented a region of interest that indicated crack propagation on PAGB, although this was not confirmed due to the super fine grain structures in the region. Section 4.4 once more presented a sub-surface initiation, but the propagation of the crack resembled a hammering impact and is consistent with the depth of the crack (150µm) and what seems an adiabatic shear band, shown in Figure 36. Furthermore, two inclusions were observed in the revealed surface, where the crack might had initiated as suggested by [8]. Finally, section 4.5 was also consistent with a crack propagating due to a hammering impact, however this crack had already reached the surface which might have affected its growth. Of special relevance in this specimen was the curvature the cracks displayed along its largest dimension and highlighted in Figure 40. Crack propagation and initiation are explained in two dimensional planes, but with a 3D model it was possible to observe its trajectory along the sample. Although the previous trends were observed from literature, further investigations are needed to decisively confirm them. However, all samples showed an interaction between cracks and inclusion regardless of the crack morphology.

6. References

[1] M. Grujicic, S. Ramaswami, R. Yavari, R. Galgalikar, V. Chenna, and J. Snipes, "Multiphysics computational analysis of white-etch cracking failure mode in wind turbine gearbox bearings," *Proc. Inst. Mech. Eng. Part L J. Mater. Des. Appl.*, vol. 230, no. 1, pp. 43–63, Feb. 2016.

[2] J. Puigcorbe and A. De-Beaumont, "Wind Turbine Gearbox Reliability," pp. 1–8, 2010.

[3] H. Polinder, "Overview of and Trends in Wind Turbine Generator Systems," in *EEE Power Engineering Society General Meeting*, 2011, pp. 1–8.

[4] H. K. D. H. Bhadeshia, "Steels for bearings," *Progress in Materials Science*, vol. 57, no. 2. Elsevier Ltd, pp. 268–435, 2012.

[5] M.-H. Evans, L. Wang, and R. Wood, "Formation mechanisms of white etching cracks and white etching area under rolling contact fatigue," *Proc. Inst. Mech. Eng. Part J J. Eng. Tribol.*, vol. 228, no. 10, pp. 1047–1062, 2014.

[6] H. Swahn, P. C. Becker, and O. Vingsbo, "Martensite decay during rolling contact fatigue in ball bearings," *Metall. Trans. A*, vol. 7, no. 7, pp. 1099–1110, 1976.

[7] J. R. Davis and A. S. M. I. H. Committee, *Carbon and Alloy Steels*. ASM International, 1996.

[8] M.-H. Evans, "An updated review: white etching cracks (WECs) and axial cracks in wind turbine gearbox bearings," *Mater. Sci. Technol.*, vol. 0836, no. March, p. 160226082749003, 2016.

[9] H. Mikami and T. Kawamura, "Influence of Electrical Current on Bearing Flaking Life," Apr. 2007.

[10] W. Holweger *et al.*, "White Etching Crack Root Cause Investigations," *Tribol. Trans.*, vol. 58, no. 1, pp. 59–69, 2015.

[11] K. Stadler, J. Lai, and R. H. Vegter, "A Review: The Dilemma With Premature White Etching Crack (WEC) Bearing Failures," *Bear. Steel Technol. 10th Vol. Adv. Steel Technol. Roll. Bear.*, no. June, pp. 1–22, 2014.

[12] H. Harada, T. Mikami, M. Shibata, D. Sokai, A. Yamamoto, and H. Tsubakino, "Microstructural Changes and Crack Initiation with White Etching Area Formation under Rolling/Sliding Contact in Bearing Steel," *ISIJ Int.*, vol. 45, no. 12, pp. 1897–1902, 2005.

[13] S. Janakiraman, O. West, P. Klit, and N. S. Jensen, "Observations of the effect of varying Hoop stress on fatigue failure and the formation of white etching areas in hydrogen infused 100Cr6 steel rings," *Int. J. Fatigue*, vol. 77, pp. 128–140, Aug. 2015.

[14] H. Polinder, F. F. A. Van Der Pijl, G. J. De Vilder, and P. J. Tavner, "Comparison of direct-drive and geared generator concepts for wind turbines," *IEEE Trans. Energy Convers.*, vol. 21, no. 3, pp. 725–733, 2006.

[15] M. H. Evans, L. Wang, H. Jones, and R. J. K. Wood, "White etching crack (WEC) investigation by serial sectioning, focused ion beam and 3-D crack modelling," *Tribol. Int.*, vol. 65, pp. 146–160, 2013.

[16] R. Luyckx, W. Etching, and C. Failure, "White Etching Crack Failure Mode in Roller Bearings : From Observation via Analysis to Understanding and an Industrial Solution," no. August, pp. 1–25, 2013.

[17] A. B. Jones, "Effect of structural changes in steel on fatigue life of bearings," *Steel*, vol. 119, pp. 68–70, 1946.

[18] J. BUCHWALD, "AN ANALYSIS OF MICROSTRUCTURAL CHANGES IN 52100 STEEL BEARINGS DURING CYCLIC STRESSING," *Asm Trans. Q.*, vol. 61, no. 4, 1968.

[19] P. C. Becker, "MICROSTRUCTURAL CHANGES AROUND NON-METALLIC INCLUSIONS CAUSED BY ROLLING-CONTACT FATIGUE OF BALL-BEARING STEELS," *Met. Technol.*, vol. 8, 1981.

[20] K. Iso, A. Yokouchi, and H. Takemura, "Research Work for Clarifying the Mechanism of White Structure Flaking and Extending the Life of Bearings," in *Sae Technical Papers*, 2005.

[21] T. Bruce, E. Rounding, H. Long, and R. S. Dwyer-Joyce, "Characterisation of white etching crack damage in wind turbine gearbox bearings," *Wear*, vol. 338–339, pp. 164–177, Sep. 2015.

[22] T. A. Harris, *Rolling Bearing Analysis, 4th Edition*, vol. 108, no. 1. 2000.

[23] K. L. Johnson and L. M. Keer, "Contact Mechanics," *J. Tribol.*, vol. 108, no. 4, p. 659, 1986.

[24] V. L. Popov, "Contact Mechanics and Friction," *Contact Mech. Frict.*, pp. 55–70, 2010.

[25] A. Vincent, "From white etching areas formed around inclusions to crack nucleation in bearing steels under rolling contact fatigue," *Astm Spec. Tech. Publ.*, vol. 1327, 1998.

[26] D. MCCORMICK, "ROLLER-BEARINGS PICK UP THE PACE," *Des. Eng.*, vol. 52, no. 5, 1981.

[27] H. K. D. H. Bhadeshia, "Steels for bearings," *Prog. Mater. Sci.*, vol. 57, no. 2, pp. 268–435, Feb. 2012.

[28] M.-H. Evans, A. D. Richardson, L. Wang, and R. J. K. Wood, "Serial sectioning investigation of butterfly and white etching crack (WEC) formation in wind turbine gearbox bearings," *Wear*, vol. 302, no. 1–2, pp. 1573–1582, Apr. 2013.

[29] S. M. Moghaddam, F. Sadeghi, K. Paulson, N. Weinzapfel, M. Correns, and M. Dinkel, "A 3D numerical and experimental investigation of microstructural alterations around non-metallic inclusions in bearing steel," *Int. J. Fatigue*, vol. 88, pp. 29–41, Jul. 2016.

[30] L. Reimer, *Scanning Electron Microscopy*. Berlin, Heidelberg: Springer Berlin Heidelberg, 1985.

[31] B. Hafner, "Energy Dispersive Spectroscopy on the SEM: A Primer," *Charact. Facil. Univ. Minnesota*, pp. 7–10, 2006.

[32] T. Maitland and S. Sitzman, “Backscattering Detector and EBSD in Nanomaterials Characterization,” in *Scanning Microscopy for Nanotechnology*, New York, NY: Springer New York, 2006, pp. 41–75.

[33] T. Nishinaga, “Handbook of Crystal Growth: Bulk Crystal Growth: Second Edition,” *Handb. Cryst. Growth Bulk Cryst. Growth Second Ed.*, vol. 2, pp. 1–1381, 2014.

[34] A. G. Rao, H. Bale, A. Merkle, and V. P. Deshmukh, “3D Investigation of the Microstructure Evolution in Hypereutectic Aluminum Silicon Alloy using High Resolution Phase Contrast X-Ray Microscopy,” *Microsc. Microanal.*, vol. 22, no. S3, pp. 1890–1891, 2016.

[35] H. K. Danielsen *et al.*, “Multiscale characterization of White Etching Cracks (WEC) in a 100Cr6 bearing from a thrust bearing test rig,” *Wear*, vol. 370–371, pp. 73–82, Jan. 2017.